الجمهورية الجزائرية الديمقراطية الشعبية
People's Democratic Republic of Algeria
وزارة التعليم العالي و البحث العلمي
Ministry of Higher Education and Scientific Research

المدرسة الوطنية العليا للتكنولوجيا و الهندسة - عنابة
National Higher School of Technology and Engineering – Annaba

In Partial Fulfillment of the Requirements

for the Degree of

STATE ENGINEER

Field of Study: Mechanical Engineering

Presented by

Ramzi BOUZIANE

PERFOMANCE OPTIMAZATION OF A MINIATURIZED CENTRIFUGAL PUMP: INNOVATIVE DESIGN AND 3D PRINTING FABRICATION

Supervised by

Dr. Slimane NIOU
ENSTI Annaba

Co-Supervised by

Dr. Naamane BENHASSINE

Department of Process Engineering and Energetics

Examination Board:

- Dr. AYAD Amar — President – ENSTI
- Pr. AZZOUZ Salaheddine — Examiner – ENSTI
- Dr. CHIHEB Sofiane — Examiner – ENSTI
- Dr. NIOU Slimane — Examiner – ENSTI
- Dr. BENHASSINE Naamane — Examiner – ENSTI
- Bendjeddou Sofiane — Guest – SIDER EL HADJAR

Academic Year 2025

Table of content

Figures list

Tables list

Acknowledgments

I would like to express my deepest gratitude to everyone who has supported me throughout my academic journey and the completion of this thesis.

First and foremost, my profound appreciation goes to my beloved parents, **BOUZIANE El Hacene** and **BELLAH Leila**. Your unwavering love, endless support, and constant encouragement throughout my life have been the foundation of my achievements. This accomplishment is as much yours as it is mine.

To my wonderful brothers and sisters, **Rym, Nassim, Karim, Hanine** and my nephew **Ihab,** thank you for your understanding, companionship, and belief in me. Your presence has always been a source of strength.

I extend a special thank you to my lifelong friends, **Hicham, Ayoub, and Ziyad**. Your enduring friendship, unwavering support, and shared memories have made this journey immeasurably richer. Your encouragement has meant the world to me.

I am also grateful to all the individuals who have had a positive impact on my life, offering guidance, inspiration, and kindness when I needed it most. Your contributions, large or small, have shaped me into the person I am today.

A warm thank you to my class, **EDD 2023-2025**, for the shared experiences, collaborative spirit, and camaraderie that made our time together truly special.

My sincere gratitude goes to my esteemed supervisor, **Dr. NIOU Slimane** and my co-supervisor **Dr. BENHASSINE Naamane**, for their invaluable guidance, insightful feedback, and unwavering support throughout this research. Your expertise and dedication have been instrumental in shaping this work.

Finally, I wish to express my appreciation to all the doctors and professors from whom I had the privilege to learn, and to all the dedicated staff of the **École Nationale Supérieure de Technologie et Ingénierie Annaba**. Your commitment to education and your contributions to my learning experience are deeply appreciated.

Abstract

This thesis addresses the challenge of optimizing miniaturized centrifugal pumps, which are critical for high-precision applications in fields like biotechnology and electronics cooling but are often limited by traditional manufacturing techniques. To overcome these limitations, this study proposes an innovative pump design that incorporates a synchronous magnetic coupling, leveraging advanced simulation and manufacturing techniques to enhance efficiency and compactness. The design process utilized SolidWorks for detailed CAD modeling and CFTurbo for hydraulic geometry generation. Performance was rigorously analyzed through a dual-simulation approach: Computational Fluid Dynamics (CFD) with ANSYS Fluent was used to optimize internal fluid flow and determine the impeller torque, while COMSOL Multiphysics was employed to simulate the magnetic coupling and ensure effective torque transmission. The final prototype was fabricated via state-of-the-art 3D printing technology, facilitating cost-effective and rapid production. Experimental testing confirmed the enhanced performance of the new pump, validating the design predictions. Most significantly, the optimized pump demonstrated an **84% average increase in pressure** and a **74% average increase in flow rate** compared to a previous design, confirming the success of the applied methods. The successful integration of these advanced methodologies underscores the pump's potential for high-precision applications and lays the groundwork for a patentable innovation with significant industrial impact.

Keywords

Miniaturized Centrifugal Pump, Performance Optimization, Magnetic Coupling, 3D Printing, Computational Fluid Dynamics (CFD), Finite Element Method (FEM)

Résumé

Ce mémoire aborde le défi de l'optimisation des pompes centrifuges miniaturisées, qui sont essentielles pour des applications de haute précision dans des domaines tels que la biotechnologie et le refroidissement de composants électroniques, mais souvent limitées par les techniques de fabrication traditionnelles. Pour surmonter ces limitations, cette étude propose une conception de pompe innovante qui intègre un accouplement magnétique synchrone, en s'appuyant sur des techniques de simulation et de fabrication avancées pour améliorer l'efficacité et la compacité. Le processus de conception a utilisé SolidWorks pour la modélisation CAO détaillée et CFTurbo pour la génération de la géométrie hydraulique. La performance a été rigoureusement analysée par une approche de double simulation : la Mécanique des Fluides Numérique (CFD) avec ANSYS Fluent a été utilisée pour optimiser l'écoulement interne du fluide et déterminer le couple de la roue, tandis que COMSOL Multiphysics a été employé pour simuler l'accouplement magnétique et garantir une transmission de couple efficace. Le prototype final a été fabriqué via une technologie d'impression 3D de pointe, facilitant une production rapide et rentable. Les essais expérimentaux ont confirmé la performance améliorée de la nouvelle pompe, validant ainsi les prédictions de la conception. De manière significative, la pompe optimisée a démontré une **augmentation moyenne de 84 % de la pression** et une **augmentation moyenne de 74 % du débit** par rapport à une conception précédente, confirmant le succès des méthodes appliquées. L'intégration réussie de ces méthodologies avancées souligne le potentiel de la pompe pour des applications de haute précision et jette les bases d'une innovation brevetable avec un impact industriel et technologique significatif.

ملخص

تتناولُ هذهِ الأطروحةِ تحدي تحسينِ أداءِ المضخاتِ الطرديةِ المصغرةِ، والتي تُعدُ ضروريةً للتطبيقاتِ عاليةِ الدقةِ في مجالاتِ مثلِ التكنولوجيا الحيويةِ وتبريدِ الإلكترونياتِ، لكنها غالبًا ما تكونُ محدودةً بسببِ تقنياتِ التصنيعِ التقليديةِ. وللتغلبِ على هذهِ القيودِ، تقترحُ هذهِ الدراسةُ تصميمًا مبتكرًا لمضخةٍ يدمجُ اقترانًا مغناطيسيًا تزامنيًا، مستفيدًا من تقنياتِ المحاكاةِ والتصنيعِ المتقدمةِ لتعزيزِ الكفاءةِ والدمجِ البنيوي.

تمَّ استخدامُ برنامجِ Solidworks لإنشاءِ نماذجَ تفصيليةً ثلاثيةَ الأبعادِ، وبرنامجِ CFturbo لتوليدِ الهندسةِ الهيدروليكيةِ للمضخةِ. وقد تمَّ تحليلُ الأداءِ بشكلٍ دقيقٍ من خلال نهجٍ مزدوجٍ للمحاكاةِ: حيثُ استُخدمَ برنامجُ Ansys Fluent في ديناميكا الموائعِ الحسابيةِ لتحديدِ عزمِ الدوران، بينما استُخدمَ برنامجُ COMSOL Multiphysics لمحاكاةِ الاقترانِ المغناطيسيِ وضمانِ نقلِ العزمِ بكفاءةٍ.

تمَّ تصنيعُ النموذجِ النهائيِ باستخدامِ تقنيةِ الطباعةِ الثلاثيةِ الأبعادِ الحديثةِ، مما أتاحَ إنتاجًا سريعًا وفعالًا من حيثِ التكلفةِ. وقد أكدتِ الاختباراتُ التجريبيةُ الأداءَ المحسنَ للمضخةِ الجديدةِ، مما دعمَ التوقعاتِ النظريةِ للتصميمِ. والأهمُ من ذلكَ، أظهرتِ المضخةُ المحسنةُ زيادةً بنسبةِ 84٪ في متوسطِ الضغطِ، وزيادةً بنسبةِ 74٪ في متوسطِ معدلِ التدفقِ مقارنةً بالتصميمِ السابقِ، مما يؤكدُ نجاحَ المنهجياتِ المطبقةِ.

وتُبرزُ عمليةُ الدمجِ الناجحِ لهذهِ الأساليبِ المتقدمةِ الإمكانياتِ الكبيرةِ للمضخةِ في التطبيقاتِ الدقيقةِ، كما تمهدُ الطريقَ لابتكارٍ قابلٍ للحصولِ على براءةِ اختراعٍ ولهُ تأثيرٌ صناعيٌ كبيرٌ.

GENERAL INTRODUCTION

The demand for compact, efficient, and precise fluid management systems has grown rapidly, driven by advancements in fields as diverse as microfluidics, biomedical devices, electronic cooling, and chemical analysis. Here, miniaturized centrifugal pumps based on magnetic coupling have emerged as star technologies due to the fact that they provide seal-less operation, which mitigates against common issues of leakage, wear, and maintenance of dynamic seals, improving operating safety and life of the pump and offering high cleanliness, a prime requirement in space-constrained, sensitive applications. This new design of pump, both the impeller and the entire hydraulic geometry, was created with much attention utilizing CFturbo's analytical models and accurate CAD modeling in SolidWorks to facilitate initial generation of geometry for specified operating conditions, and to facilitate an iterative cycle of design development with analytical predictions of leading parameters. At the same time, additive manufacturing, or 3D printing, has transformed component production with unimaginable ability to create complex geometries at incredible speed and economy. Such flexibility is especially useful in miniaturized hydraulic systems, where nuanced variations in design can have a profound effect on performance, and the ability to fabricate different configurations quickly allows for iterative design evolution and experimental testing. At the center of the seal-less operation of the pump lies the synchronous magnetic coupling, coaxial with concentric rings of permanent magnets, whose intricate behavior and high torque transmission capability were exhaustively researched by Finite Element Modeling in COMSOL Multiphysics to check if it was feasible for it to be capable of transmitting mechanical power from an external motor to the impeller, safely overcoming the operation torque computed by fluid-dynamic analysis. While experimental interrogation provides valuable empirical data, further detailed understanding of internal fluid motions, pressure distributions, and velocity patterns is generally out of reach in the absence of advanced analytical tools. Computational Fluid Dynamics (CFD) has thus become a crucial supplement to experimental testing, enabling high-fidelity visualization and meticulous analysis of complex flow behavior under a wide range of operating conditions, and such supplemental methodology makes feasible potent design optimization long before physical prototype construction. This engineering thesis integrates these frontier fields, magnetic coupling, additive manufacturing, and CFD modeling, to investigate systematically and numerically confirm the hydraulic performance of this novel 3D-printed miniature centrifugal pump. The one optimized impeller design of the pump was initially experimentally examined over a range of rotational speeds with such experiments carried out very carefully and results thereafter presented and investigated in an attempt to provide useful first impressions of pressure rise and flow rate, the aim being to develop a sound framework for future design, minimizing development cycles considerably and maximizing overall product performance. This thesis is organized into four main chapters following a clear methodological progression:

First, Chapter 1 provides a comprehensive literature review on miniature centrifugal pumps, analyzing their current advantages, limitations, and application fields.
Next, Chapter 2 details the design methodology, ranging from analytical calculations to 3D modeling in SolidWorks and hydrodynamic optimization using CFturbo.
Then, Chapter 3 presents a complete system analysis, including: Finite Element Modeling (FEM) and simulation of the magnetic coupling in COMSOL Multiphysics, Additive manufacturing of components via 3D printing and Final assembly of the functional prototype
Finally, Chapter 4 experimentally validates the prototype's performance through systematic comparison of measured results with theoretical predictions and previous pump design.
To conclude this work, a general discussion summarizes the key research contributions while proposing promising avenues for future developments...

CHAPTER I: Miniature Centrifugal Pumps: A Literature Review

I.1 Introduction

The increasing demand for compact and efficient fluidic systems in biomedical, microfluidic, and thermal management applications has driven significant advances in miniature pump technologies. Among the various types of pumps, centrifugal pumps stand out due to their mechanical simplicity, ability to deliver continuous flow, and robustness. When adapted to miniature scales, however, centrifugal pumps face unique design and performance challenges that are not encountered at the macroscale. This chapter provides a comprehensive literature review on miniature centrifugal pumps, covering their fundamental design principles, miniaturization constraints, innovative solutions involving magnetic coupling, and the integration of modern tools such as computational fluid dynamics (CFD) and additive manufacturing. This review sets the stage for the design and development approach adopted in the present work.

I.2 Centrifugal Pump Theory and Design

A centrifugal pump converts mechanical energy into fluid energy by accelerating liquid radially outward through a rotating impeller. A thorough understanding of its governing physics, the effects of scaling, and strategies for maximizing performance is essential for a robust, high-efficiency design.

I.2.1 Fundamental Principles and Governing Equations

Table 1 Pump design fundamental equations

Concept	**Equation**	**Description**
Continuity (Mass Conservation) [1]	$Q = A\,V = const$	For incompressible flow, the volumetric flow rate is conserved.
Euler's Turbomachinery Equation [1]	$H_t = \frac{1}{g}(U_2 V_{u2} - U_1 V_{u1})$	Theoretical head from the change in fluid's angular momentum.
Bernoulli's Equation [1]	$\frac{p}{\rho g} + \frac{V^2}{2g} + z = \text{const.}$	Energy conservation along a streamline (ideal flow).
Slip Factor [1]	$H = \sigma\, H_t$	Adjusts theoretical head to account for real flow deviations (slip).
Hydraulic Efficiency [1]	$\eta_h = \frac{H}{H_t}$	Efficiency that includes hydraulic losses.

Q: Volumetric flow rate

A: Cross-sectional area

V: Average velocity

H_t: Theoretical head (Euler head)

H: Actual head

U: Blade speed

V_u: Absolute tangential component of fluid velocity

ω: Angular velocity of the impeller

r: Radius

p: Pressure

ρ: Fluid density

g: Gravitational acceleration

z: Elevation

σ: Slip factor

η_h: Hydraulic efficiency

Subscripts 1 and 2: Refer to inlet and outlet conditions, respectively.

I.3 Miniature and Micro-Pump Technologies

The demand for miniature and micro-pumps has grown significantly across microfluidics, biomedical, and electronics cooling applications [2], [3] . These pumps fall into two primary categories:

1. Non-mechanical pumps: Utilize physical phenomena to move fluid without moving parts (e.g., electrokinetic or electrohydrodynamic pumps) [4].
2. Mechanical pumps: Employ solid moving components to displace fluid [4], further classified as:
    - *Positive displacement pumps* (precise but pulsatile flow, e.g., peristaltic or diaphragm pumps) [5], [6], [7].
    - *Dynamic pumps* (continuous flow, such as centrifugal pumps) [8].

Miniature centrifugal pumps offer distinct advantages [8], [9], [10], [11]:

✓ Continuous, stable flow (critical for biomedical applications) [2], [9], [11].

✓ Mechanical simplicity (single rotating component: the impeller)[10].

✓ High flow capacity (milliliters/liters per minute vs. microliters)[3], [11].

However, centrifugal pump miniaturization presents well-documented scientific challenges. Pump performance does not scale linearly with size, as conventional affinity laws become inaccurate at small scales. Experimental studies by Kearney et al. (2009) demonstrated significant hydrodynamic efficiency degradation in geometrically similar miniaturized pumps [12]. This results from shifting fluid dynamics: in micro-scale flow channels, lower Reynolds numbers make viscous forces dominant over inertial forces, leading to:

• **Increased frictional losses**: Boundary layers occupy proportionally larger flow areas, reducing hydraulic efficiency[12], [13].
• **Hemolysis risk**: High shear stresses may damage red blood cells in biomedical applications[9], [14].
• **Complex flow patterns**: Secondary flows, vortices, and dead zones disrupt ideal fluid paths [12], [15].

To address these limitations, innovative designs have emerged:

- **Optimized impeller geometries** (increased blade count and outlet angles) [12], [15].
- **Magnetic levitation systems** (eliminating shafts and bearings to reduce mechanical losses) [2]

I.4 Pump Designs & Magnetic Couplings

A primary motivation for innovation in modern pump design is the elimination of dynamic seals, which are a common point of failure, leakage, and contamination. In applications within the biomedical, pharmaceutical, or chemical processing industries, ensuring the hermetic containment of the working fluid is paramount [16], [17].

Magnetic couplings can be broadly categorized as either **asynchronous** or **synchronous** based on their operating principle as shown in Figure 1 [18]. Asynchronous couplings function based on a speed differential, or "slip," between the driving and driven rotors. For instance, an eddy-current coupling uses a rotor with permanent magnets to induce currents in a conductive drum on the opposing rotor. The interaction between the resulting magnetic fields generates torque, but this process is inherently lossy and generates significant heat [19].

In contrast, a **synchronous magnetic coupling (figure…)**. This design consists of two concentric rotors (an inner and an outer) fitted with an equal number of high-strength permanent magnets, typically rare-earth magnets like Neodymium-Iron-Boron (NdFeB) or Samarium-Cobalt (SmCo) for their high magnetic energy product [20]. These magnets are arranged in an alternating polarity pattern (N-S-N-S) on each rotor. As the external driving rotor turns, its magnetic field interacts with the magnets on the internal driven rotor, creating forces of attraction and repulsion that cause it to rotate in perfect synchrony (1:1 speed ratio) with no slip [16]. This configuration is favored for its high efficiency and robust torque capacity [18], [20]. The maximum transmissible torque, often called the "pull-out torque," is a critical design parameter determined by the magnetic material properties. If the operational load torque exceeds this pull-out torque, the magnetic lock between the rotors will decouple, and power transmission will cease [17], [21].

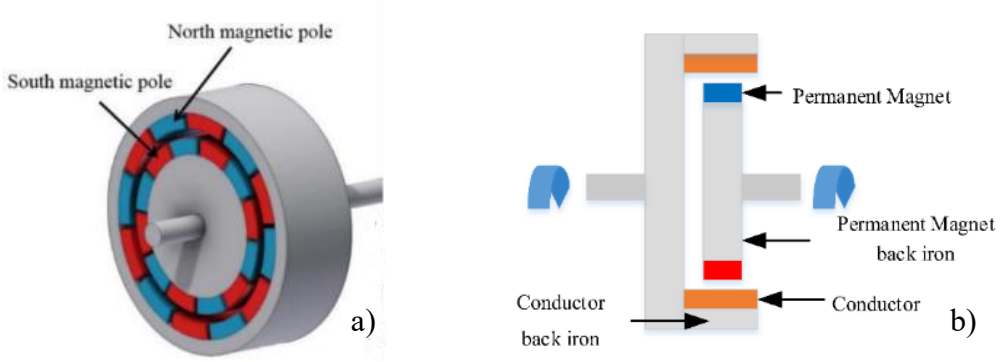

Figure 1 Illustration of a) synchronous magnetic coupling b) asynchronous magnetic coupling[18]

The successful application of magnetically coupled centrifugal pumps, leveraging these principles, has been demonstrated in several recent studies. The combination of magnetic coupling with advanced fabrication methods has proven particularly fruitful. Jo et al. (2022) developed a 3D-printed miniature centrifugal pump with non-contact magnetic actuation for applications in microfluidics and biological analysis [2]. In a similar vein, Joswig et al. (2019) demonstrated a technique to embed permanent magnets directly into the pump rotor during the 3D printing process, creating a monolithic, multi-material component that simplifies assembly and enhances the integration of functional elements [22]. These studies underscore the viability and timeliness of combining magnetic coupling with modern design and manufacturing tools to create innovative pumping solutions.

I.5 Computational Fluid Dynamics (CFD) in Pump Design

Modern turbomachinery development relies heavily on the use of Computational Fluid Dynamics (CFD) to analyze and optimize designs prior to physical prototyping. This numerical approach solves the governing equations of fluid motion (the Navier-Stokes equations) to predict performance metrics such as head, flow rate, and efficiency. More importantly, CFD provides detailed insight into the complex internal flow structures within the pump, such as velocity distributions, pressure fields, and the formation of recirculation zones or vortices, which are often difficult and expensive to measure experimentally[11], [23], [24].

The use of CFD has become a standard validation step in pump design literature. Patil et al. (2019) utilized CFD to validate the performance of a 3D-printed centrifugal pump, confirming that numerical simulations can accurately predict experimental outcomes[25]. Kearney et al. (2009) highlighted the importance of CFD in understanding the fluidic loss mechanisms that arise during pump miniaturization, where phenomena like secondary flows become more prominent [12].

I.6 Additive Manufacturing for Prototyping

The emergence of additive manufacturing, commonly known as 3D printing, has revolutionized the process of fabricating complex mechanical components. For the development of miniature pumps, this technology offers several distinct advantages over traditional manufacturing methods like machining or molding. The primary benefit is the ability to create highly complex and optimized geometries, such as curved impeller blades and intricate volute passages, with relative ease and at low cost [25]. This design freedom allows for rapid prototyping, where multiple design iterations can be fabricated and tested in a short period of time to achieve optimal performance [23]

The suitability of 3D printing for miniature pump fabrication is well-established in recent literature. Several researchers have successfully created and tested 3D-printed centrifugal pumps for various applications [23][2]. Joswig et al. (2019) demonstrated a particularly advanced application of the technology by embedding permanent magnets directly into the pump rotor during the 3D printing process. This "print-pause-print" technique enables the creation of a monolithic, multi-material component, simplifying assembly and enhancing the integration of functional elements[22].

I.7 Conclusion

This chapter reviewed the key principles and challenges of miniature centrifugal pump design. It emphasized the impact of miniaturization, and the relevance of CFD and 3D printing in optimizing performance. These insights support the methodology adopted in this project to develop an innovative and efficient mini pump.

CHAPTER II: DESIGN AND MODELLING OF THE MINIATURE CENTRIFUGAL PUMP

II.1 Introduction

This chapter details the comprehensive design process for the miniature centrifugal pump, beginning with the definition of key operational targets for flow rate and head. It outlines the use of CFturbo to establish the initial hydraulic geometry based on fundamental engineering principles and performance indicators. The subsequent sections elaborate on the specific design choices for the impeller and volute, balancing theoretical calculations with the practical constraints of additive manufacturing to create a robust and efficient model ready for simulation and fabrication.

II.2 Design of the Miniaturized Centrifugal Pump

II.2.1 Global setup and initial objectives

The design aimed to develop a compact centrifugal pump capable of delivering **3.5 L/min** of water at a **head of 0.4 m**, with an operational speed of **2500 RPM**. These values reflect the working range of a miniaturized water pump targeted for low-head, low-flow applications. A key objective was to achieve an **impeller diameter around 26 mm**.

Once these design parameters are defined, the software automatically computes several essential performance indicators, these quantities serve as the foundation for the remainder of the design process. They influence component sizing, blade layout, and overall flow distribution. Table 1 summarizes, in equation form, the key indicators used to size and evaluate a centrifugal pump.

Table 2 key performance indicators calculated using empirical and dimensional analysis methods

Equation	Description	Uses
$\boldsymbol{n_s = \frac{n \cdot \sqrt{Q}}{(gH)^{3/4}}}$	Specific speed	Classifies pump type (radial/mixed/axial)
$\boldsymbol{\delta = \frac{d_2 (gH)^{1/4}}{Q^{1/2}}}$	Specific diameter	Determines appropriate impeller size
$\boldsymbol{P = \rho g\, Q\, H}$	Hydraulic power output [W]	Power delivered to the fluid
$\boldsymbol{\Delta p = \rho g H}$	Pressure increase [Pa]	Total pressure rise through the pump
$\boldsymbol{u_2 = \frac{\pi d_2 n}{60}}$	Impeller tip speed [m/s]	Needed for velocity triangle and head
$\boldsymbol{\psi = \frac{gH}{u_2^2}}$	Work coefficient	Describes energy added to fluid per unit tip speed
$\boldsymbol{\phi = \frac{Q}{n d_2^3}}$	Flow coefficient	Describes flow capacity relative to impeller geometry

n: Rotational speed [rev/min]
Q: Flow rate [m³/s]
H: Total head [m]
g: Gravitational acceleration [9.81 m/s²]
d_2: Impeller outlet diameter [m]
u_2: Peripheral speed at the outlet [m/s]
$P\rho$: Fluid density [kg/m³]

II.2.1 Impeller Design

II.2.1.1 Geometric Constraints

Design was effective within the confines of 3D printing. A structural stability minimum of 1 mm wall thickness was used to guarantee that the structural integrity would not be affected by the fabrication process. The blades of the impeller were set as a minimum thickness of 0.8 mm to provide an optimal balance between material durability and fluid efficiency. Due to the low forces in micro-scale applications, this was felt to be sufficient to handle operating stresses. Moreover, a short hub design was selected instead of a traditional full-length hub. This choice was done to minimize inlet blockage, decrease entrance losses, and make the geometry of the impeller easier for additive manufacturing.

II.2.1.2 Main dimensions

The software uses Euler's turbomachinery equation:

$$gH = U_2 c_{u2} - U_1 c_{u1} \tag{2.1}$$

At the outlet radius R_2 the blade speed is $U_2 = \omega R_2$ With no inlet whirl ($c_{u1} = 0$), it computes $c_{u2} = gH/U_2$, then derives the meridional flow velocity from continuity equation (2.2):

$$Q = A\, c_m \tag{2.2}$$

The impeller width b_2 and inlet diameter d_1 are adjusted to give the desired flow at this velocity.

II.2.1.3 Velocity triangles

The flow at the inlet and outlet is described by velocity triangles and demonstrated in Figure 2. At the inlet, the absolute velocity c_1 has no tangential component ($c_{u1} = 0$ swirl angle 90°), so $c_1 = c_{m1} = Q/A_1$.

The blade inlet angle β_{1B} is chosen so the relative inlet velocity w_1 meets the geometry without incidence. With the blade speed U_1 at the inlet radius, $\tan\beta_{1B} = c_{m1}/U_1$. The default is zero incidence (β_{1B} is set so c_1 enters parallel to the blade). Its manual notes that *"Calculation of β_{1B} inside CFturbo gives inflow without incidence"* and recommends keeping $\beta_{1B} < 40°$ for pumps.

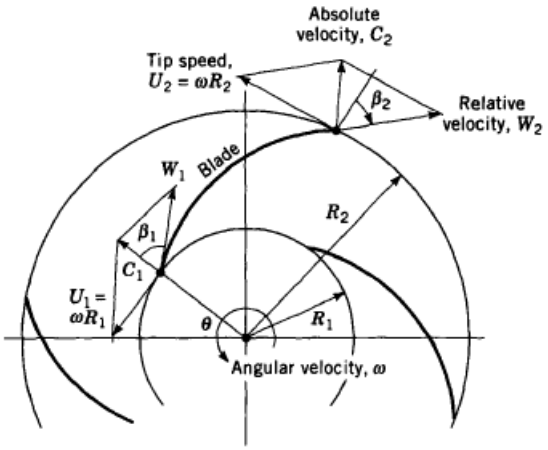

Figure 2 Relative and absolute flow velocity vectors in a rotating impeller.[1]

At the outlet, the absolute velocity c_2 has components c_{m2} (radial/meridional) and c_{u2} (tangential). From Euler, $c_{u2} = gH/U_2$. The relative outlet velocity w_2 then has $w_{u2} = U_2 - c_{u2}$ (the slip velocity) and $w_{m2} = c_{m2}$. The blade outlet angle β_{2B} is measured between w_2 and the tangential direction, so $\tan\beta_{2B} = w_{m2}/w_{u2}$. Importantly, due to slip the actual flow angle β_2 (direction of w_2) is smaller than the blade angle β_{2B}. It is emphasized that *"the relative flow angle β_2 is always smaller than blade angle β_{2B} due to the slip velocity"*. The difference $\delta = \beta_{2B} - \beta_2$ is the deviation caused by slip, the resulted velocity triangle is shown in Figure 3.

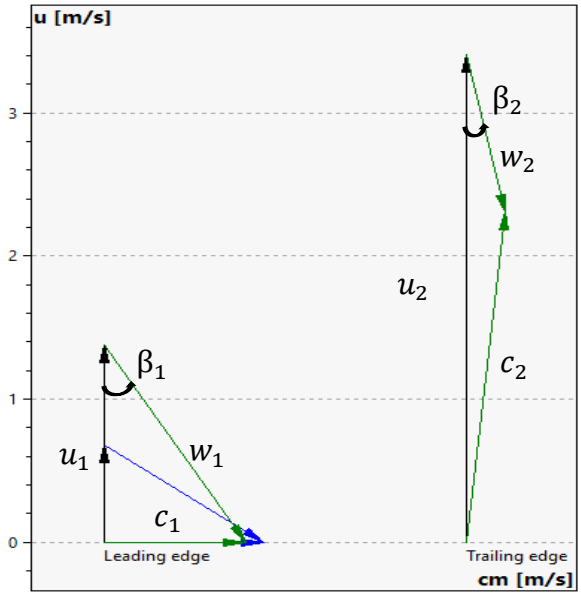

Figure 3 velocity triangle at the leading and trailing edges

II.2.1.4 Slip factor (Gülich/Wiesner)

Real impellers exhibit "slip", meaning the fluid leaves with less whirl than the blades impose. The software uses the empirical Wiesner slip factor model (with Gullich corrections) to estimate the outflow coefficient γ (analogous to slip factor). A smaller γ means more slip (larger deviation). In general, slip depends on the number of blades z, blade angles, and flow: more blades give better guidance (higher slip factor) up to a point. Stodola's formula (from turbulence theory) shows

$$\sigma = 1 - \frac{\pi}{z(1 - \phi_2 \cot\beta_2)} \tag{2.3}$$

predicting that σ rises with blade count z and decreases with more radial flow (through φ_2).

II.2.1.5 Blade angles and count

The inlet blade angle β_{1B} is computed for no incidence. Pumps usually have low β_{1B} (often *outlet blade angle* β_{2B} is chosen to satisfy the head requirement via Euler's equation); The number of blades affects these angles through slip, so one can afford a slightly smaller β_{2B} for the same head. Too few blades increase slip, requiring a larger β_{2B} (aggressive curvature) to achieve the head. In summary, blade angles are tightly linked to the velocity triangle:

$$\beta_{1B} = arctan\left(\frac{c_{m1}}{U_1}\right) \beta_{2B} = arctan\left[\frac{(U_2 - c_{u2})}{c_{m2}}\right], \tag{2.4}$$

with c_{u2} reduced by slip.

II.2.1.6 Key Performance and geometric Results for the Impeller

These results shown in Table 3 provide the basis for evaluating the performance and sizing of subsequent components such as the blade geometry and volute.

Table 3 Key performance results for the miniature centrifugal pump

Result Parameter	Symbol	Value	Unit
Specific Speed (EU)	n_s	38.0	-
Specific Diameter	δ	5.05	-
Flow Coefficient	φ	0.032	-
Head Coefficient	ψ	0.677	-
Tip Speed	u^2	3.4	m/s
Tangential Velocity at Outlet	c_{u2}	2.3	m/s
Meridional Velocity at Outlet	c_{m2}	0.2	m/s
Pressure Increase	Δp	~3.9	kPa
Hydraulic Power	P_{hyd}	~0.23	W
Required Shaft Power	P_{shaft}	~0.46	W

Based on the design point and specific speed, the impeller diameter was selected to be approximately 26 mm. The software adjusted associated parameters to match the specified operating point. The final set of main dimensions in Table 4 and angles used in the impeller design in Table 5, with the resulted geometry shown in Figure 4:

Table 4 Main dimensions values of the impeller

Parameter	Symbol	Value	Unit
Impeller Outlet Diameter	d_2	26.0	mm
Impeller Inlet Diameter	d_1	10.0	mm
Outlet Blade Width	b_2	4.5	mm
Inlet Blade Width	b_1	2.5	mm
Number of Blades	z	6	-
Blade Thickness	-	0.8	mm

Table 5 Impeller β_{B1} and β_{B2}°angles

Span		$\boldsymbol{\beta_{B1}}^\circ$	$\boldsymbol{\beta_{B2}}^\circ$
Hub	1	52.3	22.1
Middle	2	50.4	22.1
	3	45.5	22.1
	4	37.2	22.1
Shroud	5	29.7	22.1

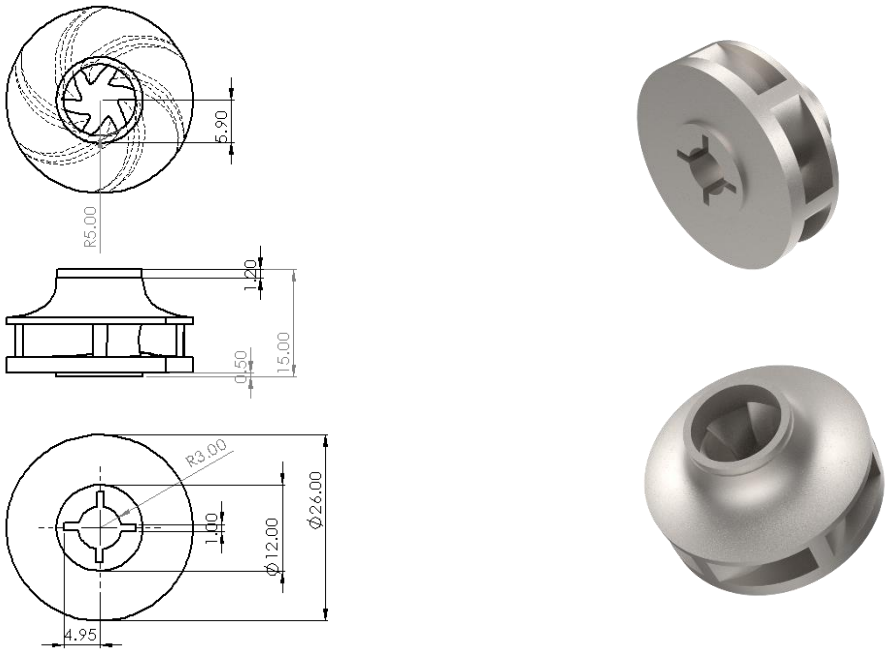

Figure 4 Technical drawing and render of the final impeller geometry

II.2.2 Volute Design

The flow field was computed according to the Pfleiderer velocity-based design approach, which prescribes the progression of spiral area based on local tangential velocity. This ensures that the exit flow from the impeller is smoothly directed along the volute passage without generating sudden changes in velocity and direction that may lead to flow separation or pressure fluctuations.

The gradually increasing volute flow cross sections are calculated from the flow rate and from an average velocity at the volute cross section center as illustrated in Figure 5 with the main dimensions shown in Table 6. The volute cross section *A* as a function of the circumferential angle *0* counted from the tongue becomes[1]:

$$A(\theta) = \frac{\theta}{2\pi} \cdot \frac{Qr}{C_{u2} \cdot R_2} \tag{2.5}$$

$A(\theta)$	Volute cross-sectional area at circumferential angle θ
Θ	Wrap angle from the tongue (cutwater), in radians (0 to 2π)
Q	Volume flow rate [m³/s] from the impeller
C_{u2}	Tangential component of absolute velocity at the impeller outlet [m/s]
R_2	Radius at impeller outlet (impeller tip radius) [m]
R	Local radius at which the volute cross-section is taken [m]
2π	Full circular angle in radians (used to normalize over 360°)

Table 6 Key Design Dimensions of the volute

Feature	Symbol	Value	Unit	Remarks
Spiral wrap angle	ϕ	360	°	Full wrap for uniform flow collection
Inlet radius	r_{in}	15	mm	Matches impeller outlet radius
Inlet width	b	7.5	mm	Compatible with impeller blade span
Outlet diameter	D_{out}	8	mm	Diffuser discharge diameter
Outer radius	r_{out}	20.1	mm	Outer radius of volute flow path

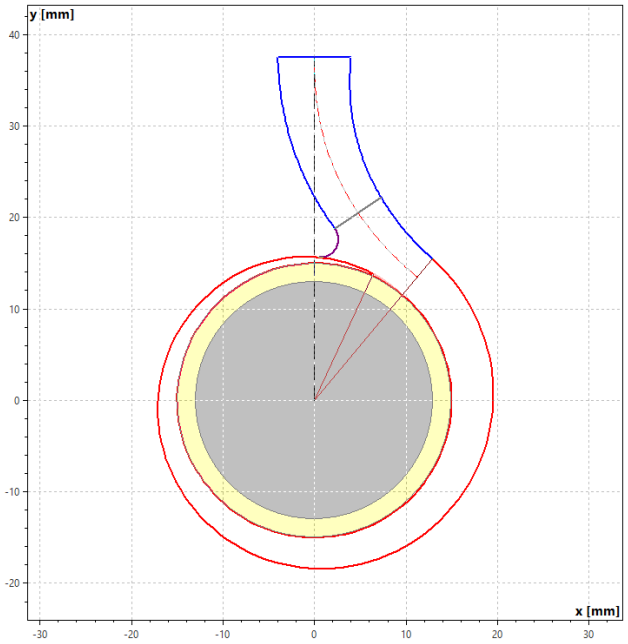

Figure 5 2D illustration of the volute geometry

II.3 Global performance of miniature centrifugal Pump

The software CFturbo automatically computes several efficiencies after which we can calculate the values shown in Table 7:

- **Hydraulic efficiency η_h:** 50% (Ratio of ideal pump work to actual fluid work).
- **Volumetric efficiency η_v:** 89.4% (Accounts for leakage/backflow through blade clearances).
- **Mechanical efficiency η_m:** 80.9% (Accounts for mechanical losses).
- **Motor efficiency η_{mot}:** 80% (Efficiency of the driving motor).

Table 7 Derived values from calculated efficiencies

Parameter	Expression	Value

Delivered Hydraulic Power ($\boldsymbol{P_{del}}$)	$P_{del} = \rho \cdot g \cdot Q \cdot H$	≈ 0.23 W
Required Shaft Power ($\boldsymbol{P_{req}}$)	$P_{req} = P_{del} / \eta_h$	≈ 0.46 W
Input Power incl. Mechanical Losses ($\boldsymbol{P_{in}}$)	$P_{in} = P_{req} / \eta_m$	≈ 0.57 W
Electrical Input Power	$P_{motor} = P_{in} / \eta_{mot}$	≈ 0.7 W
Rounded Input Power	$P_{rounded} \approx P_{motor} + margin$	~1 W
Overall Stage Efficiency ($\boldsymbol{\eta_{stage}}$)	$\eta_{stage} = \eta_h \times \eta_v \times \eta_m$	≈ 36%
Global Efficiency (incl. motor)	$\eta_{global} = P_{del} / P_{rounded}$	≈ 23%

II.4 Validation Parameters

To ensure the design is viable, key nondimensional parameters are checked.

II.4.1 The Reynolds number

$$Re = \frac{\rho V D}{\mu} \tag{2.6}$$

The Renolds number is estimated using hydraulic diameters and blade speeds. For example, at the impeller outlet: ($D_2 = 26mm$, $U_2 \approx 3.4\ m/s, \nu \approx 1 \times 10^{-}6\ m^2/s$)

$$Re \approx \rho U_2 D_2/\mu \sim 9 \times 10^4$$

Re based on inlet: $d_1(\sim 10\ mm)$ was

$$Re \approx 1.3 \times 10^4.$$

These indicate laminar/transition flow at inlet but fully turbulent flow at the outlet, as expected.

II.4.2 Net Positive Suction Head (NPSH)

Net Positive Suction Head is critical to avoid cavitation. CFturbo offers several empirical estimates. It reported an available NPSH of ~9.98 m (static 1 bar inlet) and calculated required NPSH via Pfleiderer, Petermann, Stepanoff, etc. For this design the required NPSH was minuscule (~0.03–0.10 m). Thus, cavitation is unlikely under normal conditions

II.5 Integrated Assembly Design

Figure 6 shows a 3-D exploded view of the miniature centrifugal pump, offering a detailed visual breakdown of all individual components before assembly. This type of view is particularly useful to understand how the internal parts are arranged and how they fit together within the compact housing.

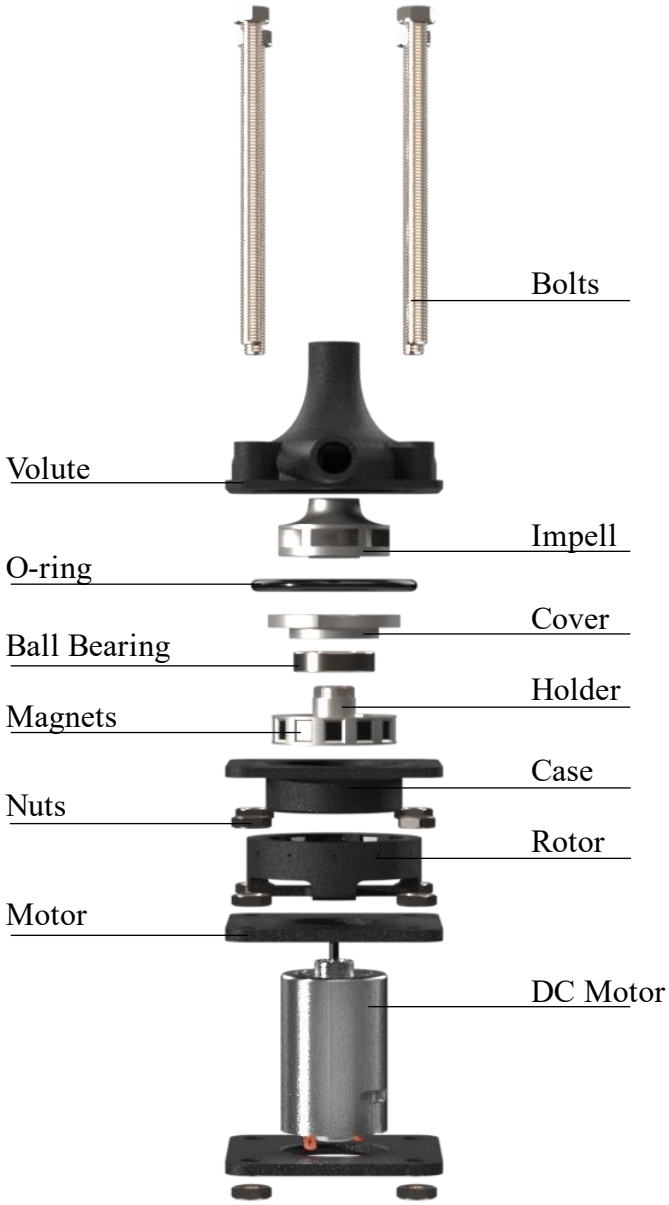

Figure 6 Render of exploded of the pump showing various component

The structural and assembly components of the pump are as follows:

- **Bolts:** fasten and hold together various components (M5).
- **Volute:** converts fluids high-velocity energy into pressure energy.
- **Case:** enclosing internal components.
- **Motor Holder:** securely hold and position the DC Motor(12V).
- **Nuts:** used with the bolts to tighten and secure parts(M5).
- **Impeller:** the primary component responsible for the pumping action.
- **Rotor:** the rotating part of the motor assembly that the magnets are attached to.
- **DC Motor:** the power source of the pump.
- **Magnets:** permanent magnets provide the magnetic coupling.
- **O-ring:** used to create a watertight geometry(39mm).
- **Ball Bearing:** low-friction support for the rotating parts(6800-2Z).
- **Cover:** separate impeller and magnet regions inside the pump.
- **Holder:** hold the magnets in place, ensuring their correct positioning.

The final design represents a compact and robust assembly, housing all necessary components for a magnetically coupled centrifugal pump. The complete CAD model, rendered to show the final product as it would be assembled, is presented below in Figure 7.

Figure 7 3D render of the final assembled parts

II.6 Conclusion

This chapter successfully translated theoretical objectives into a viable physical design. Through the systematic application of analytical models, a complete pump geometry, including the impeller and volute, was developed and detailed. The design was validated by checking critical non-dimensional parameters like the Reynolds number and NPSH, which confirmed the soundness of the hydraulic configuration. The integrated assembly showcases a compact and manufacturable pump, establishing a solid foundation for the subsequent analysis of the magnetic coupling and the physical prototyping stage

CHAPTER III:
MAGNETIC COUPLING AND 3D-PRINTED MINIATURE CENTRIFUGAL PUMP

III.1 Introduction:

This chapter focuses on two critical aspects of the pump's realization: the magnetic power transmission and the physical fabrication. It first addresses the design and analysis of the synchronous magnetic coupling, which is essential for the pump's seal-less operation. A Finite Element Model is developed in COMSOL Multiphysics to ensure the coupling can transmit the required torque with a significant safety margin. The second part of the chapter details the additive manufacturing process used to fabricate the pump components from the finalized CAD models.

III.2 Magnetic Coupling

The required magnetic coupling torque at peak should be greater than the torque required by the impeller to operate at the design point. This operating torque, arising due to fluid-dynamic drag and pressure forces on the rotating impeller, was determined from the (CFD) simulation

Torque from the CFD simulation was 0.00475 Nm. (view appendix B).

But for practical application of engineering, it would lead to failure to size the coupling to precisely this value. For durable and reliable performance, there needs to be a considerable margin of safety to account for:

- **Startup Transients:** Additional torque will be required to overcome the static friction.
- **Off-Design Conditions:** The pump may be operated at off-design flow rates.
- **Fluid Property Changes:** Fluid temperature and viscosity changes.
- **Avoiding Decoupling:** ensures abrupt pressure surges or transitory blockages don't cause the magnetic lock to "slip" or "pull-out".

For the purpose of this project, a safety factor of approximately **10x or higher** was targeted.

The target transmissible torque for the magnetic coupling was set at approximately **0.04 N.m.**

III.2.1 Magnetic Coupling Finite Element Model (FEM)

A comprehensive 3D finite element model was constructed in COMSOL Multiphysics to accurately predict the torque transmission characteristics of the coupling.

Model Geometry and Domains

The design is a **coaxial synchronous coupling**, featuring two concentric rings of permanent magnets shown in Figure 8.

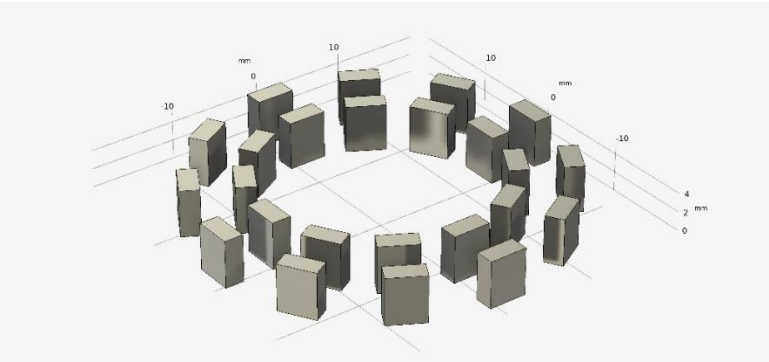

Figure 8 Coaxial synchronous magnetic coupling geometry

- The **Driving** magnets are the **outer** ring
- The **Driven** magnets are the **inner** ring

The geometry was defined parametrically based on the physical constraints of the pump assembly and the dimensions of the selected magnets. The simulation model consists of 12 outer magnets (5x4x2 mm) and 12 inner magnets (5x4x2 mm) arranged in a circular pattern with alternating magnetic polarity. To simulate rotation, the model was built as a COMSOL assembly. This allows the use of an Identity Boundary Pair to define the interface between the stationary and rotating domains, which is essential for the moving mesh functionality, the parameters chosen for this simulation are shown in Table 10.

Table 8 Key geometric parameters of the magnetic coupling

Parameter	Value
Number of Magnet Pairs	12
Inner Magnet Ring Radius (to center)	13.9 mm
Outer Magnet Ring Radius (to center)	17.2 mm
Radial Gap (between magnet faces)	4 mm

III.2.2 Material Properties and Physics

The choice of material is critical for achieving high torque density. The simulation was based on commercially available **Neodymium (NdFeB)** permanent magnets with its properties shown in Table 11.

Table 9 Magnetic Material and Simulation Properties

Magnet Grade	Remanent Flux Density (B_r)	Recoil Permeability (μ_r)	Surrounding Medium
Sintered NdFeB, Grade N54	1.4 T	1.05	Air with relative permeability of 1

The simulation was performed using the **Magnetic Fields, No Currents** physics interface. This interface is suitable for magnetostatics problems where the magnetic field originates from permanent magnets rather than electric currents. It solves for the magnetic scalar potential, V_m, governed by the equation

$$\nabla.(\mu_0\mu_r H - B_r) = 0, \quad (3.1)$$

$$\text{where } H = -\nabla V_m \quad (3.2)$$

∇ Nabla operator

μ_0 Permeability of free space (vacuum), $\approx 4\pi \times 10^{-7}$ H/m

μ_r Relative permeability of the material (dimensionless)

H Magnetic field intensity vector (A/m)

B_r Remanent magnetic flux density (from a permanent magnet), in tesla (T)

V_m Magnetic scalar potential (A)

∇V_m Gradient of the magnetic potential field

III.2.3 Meshing Strategy

A physics-controlled mesh was generated with specific refinements to ensure solution accuracy. The final mesh consisted of **135,664 domain elements** in total, with a minimum element quality of 0.05 to prevent numerical errors. A finer mesh was applied to the magnet domains and the surrounding air gap, as this is where the magnetic field gradients are steepest and the torque-transmitting forces are generated. The magnet domains were meshed using a swept mesh of hexahedra where possible, while the remaining domains were meshed with free tetrahedra as shown in figure 9

III.2.4 Solver and Study Configuration

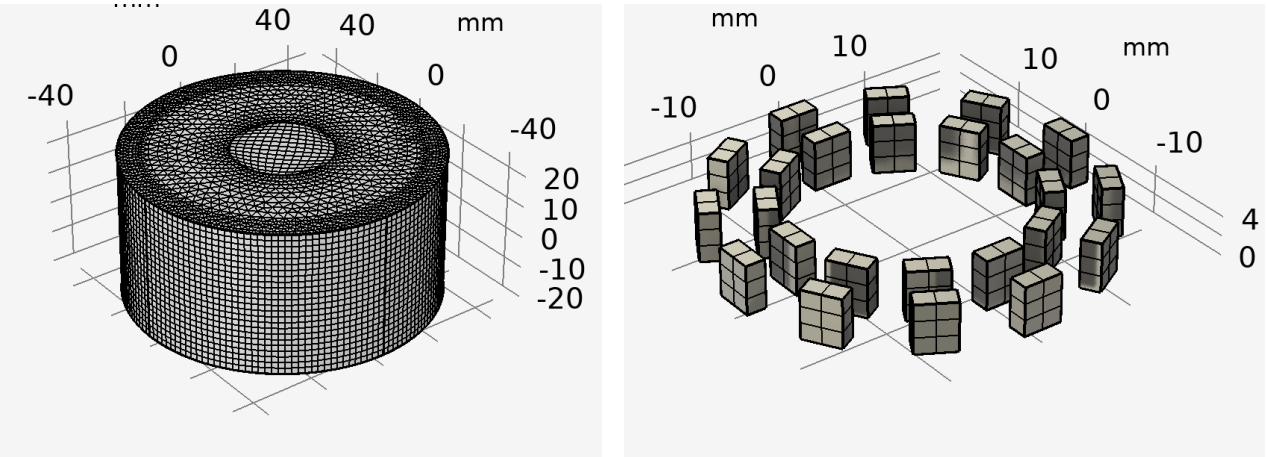

Figure 9 mesh result for the magnetic coupling simulation

To determine the maximum transmissible torque, a Stationary Study was configured with a Parametric Sweep.

- **Moving Mesh:** The **Rotating Domain** feature was applied to the outer rotor assembly to simulate its rotation relative to the outer rotor.
- **Parametric Sweep:** The parameter alpha, representing the angular displacement between the driving and driven rotors, was swept from 0 to 60 degrees. This range is sufficient to capture the full sinusoidal torque profile for a 12-pole configuration.
- **Force/Torque Calculation:** The torque was calculated at each angular step by integrating the Maxwell stress tensor over the surface of the magnet domains. COMSOL's built-in **Force Calculation** feature was applied to both the inner and outer magnet sets.

III.2.5 Simulation Results and Analysis

The parametric study provides a detailed understanding of how the transmitted torque varies with the alignment of the rotors as shown in Figures 10, 11, 12, 13.

Flux Density and Scalar Potential at Different Angles

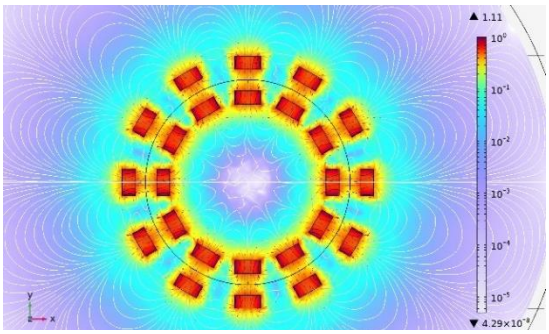

Figure 12 Flux density at 0°

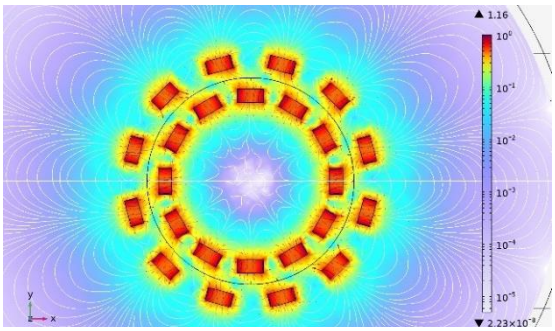

Figure 13 Flux density at 15°

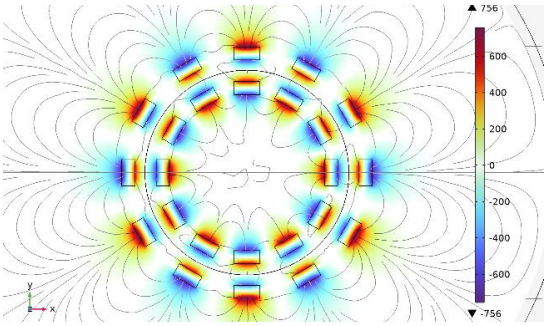

Figure 10 Scalar potential at 0°

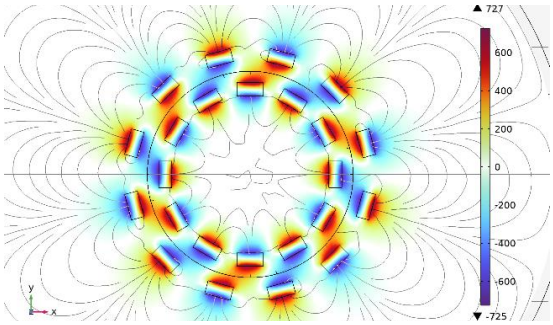

Figure 11 Scalar potential at 15°

Analysis of Flux Density and Scalar Potential results

Aligned Position (0°)

At perfect alignment, the magnetic flux density and scalar potential exhibit a synchronized symmetric distribution that demonstrates fundamental electromagnetic equilibrium, with flux density reaching maximum values of 1.11 Tesla around each permanent magnet while scalar potential oscillates symmetrically between +756 A and -756 A. The relationship between flux density regions (red zones) correspond precisely to areas of steep scalar potential gradients, with circular flux lines correlating directly with concentric potential contours to confirm uniform radial energy distribution. This symmetric distribution creates perfect electromagnetic force balance where each magnet experiences identical radial forces with purely radial potential gradients, resulting in zero tangential electromagnetic stress components.

Misaligned Position (15°)

The 15° angular displacement transforms both electromagnetic field distributions simultaneously, creating flux density intensification to 1.16 Tesla with scalar potential range shifting to ±727 A and significant spatial. The correlation between flux density asymmetry and scalar potential gradient distortion reveals that regions of flux compression and intensification (yellow-red zones) correspond to steep, non-radial potential gradients, creating tangential electromagnetic forces. These coupled field distortions create electromagnetic stress concentration zones appearing as elongated distortions in both field maps, indicating maximum torque-producing force locations. The asymmetric flux distribution increases magnetic energy storage while distorted scalar potential creates electric field components that interact with magnetic fields.

III.2.6 Maximum Transmissible Torque Analysis

The result of the parametric sweep is the characteristic torque-angle curve for the synchronous coupling, as shown in Figure 14:

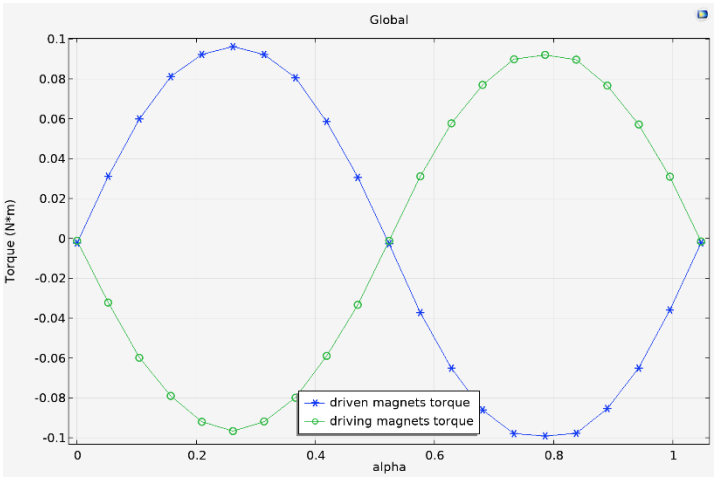

Figure 14 Torque calculation result of driven and driving magnets at different angles

The plot illustrates the torque on both the driven (inner) and driving (outer) magnets. As predicted, the transmitted torque follows a sinusoidal relationship with the angular displacement. The torque is zero when the poles are perfectly aligned (alpha = 0) and increases to a maximum value before decreasing again. This peak represents the **maximum static torque**, often called the "pull-out torque." If the load torque from the impeller exceeds this value, the magnetic coupling will break synchronicity and slip.

Based on the global evaluation of the force calculation feature in COMSOL, the maximum calculated torque on the driven rotor was determined to be:

Maximum Transmissible Torque = 0.102 N·m

This simulated result demonstrates that the designed coupling is exceptionally robust. Comparing this to the required hydraulic torque of 0.04 N·m, the achieved safety factor is well in excess of the 10x target. Table 11 shows the maximum toque and slip angle for different configurations:

Table 10 Maximum torque and slip angles results at different magnets count

Number of magnets	Slip angle [°]	Maximum torque [N.m]
4	80	0.023
8	33	0.044
12	15	0.102
16	12.5	0.143

- 4 magnets: lower than the targeted torque value.
- 8 magnets: the toque is sufficient but the slip was deemed too high for a stable system.
- 12 magnets: sufficient torque and reasonable slip angle.
- 16 magnets: sufficient torque and reasonable slip angle.

This confirms that the selected configuration of 12 pairs, the number of the magnets also adds to the moment of inertia due to the extra weight of the magnets provide, making the impeller

more stable at higher operating speeds. This leads us to designing the geometry of the holder suitable for this configuration in figure 15:

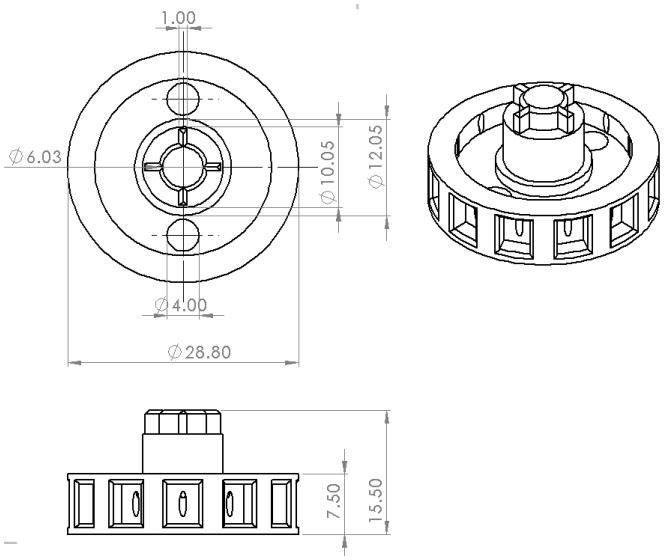

Figure 15: Holder

III.3 Manufacturing Using 3D Printing

The next part explains the steps involved in printing ABS using Anycubic 3D printers and Ultimaker Cura software, including post-processing techniques using alcohol and UV curing, the equipment listed in Table 9 and shown in Figure 16:

Table 11 List of 3D-Printing equipment

3D Printer	Anycubic Photon Mono 4K
Resin Type	ABS-Like Resin
Slicing Software	Ultimaker Cura
Additional Tools	Adhesive for the print bed, Tweezers, Scraper
Post-Processing Tools	Isopropyl Alcohol (IPA), Anycubic Wash and Cure Machine

Figure 16 3-D printing Process: a) ABS-Like Resin, b) Anycubic Photon Mono 4K c) Cure Machine d) Anycubic Wash

Printing process

The 3D printing process starts off by exporting the SolidWorks-designed geometry in STL format. The file is loaded into Ultimaker Cura, where the model is correctly oriented onto the build plate to achieve stability and have sufficient clearance from other parts. The support structures are automatically generated by the software, the calculated volume of resin needed is estimated, as well as an estimated total print time.

Once these settings are done, the print file is exported and sent to the Anycubic Photon Mono 4K printer. Before printing begins, the required amount of ABS-like resin is poured into the vat of the printer. The printer then carries out the printing process according to the prepared file. After printing, the printed parts are removed carefully from the build platform. Post-processing begins with the manual removal of support structures using tweezers and a scraper. Then the parts are cleaned using isopropyl alcohol (IPA) to eliminate any residual resin. Finally, the printed parts are UV cured in a specialized curing machine for complete polymerization and mechanical stability for 3 minutes, which gives us at the end the final printed parts for the centrifugal pump in Figure 17:

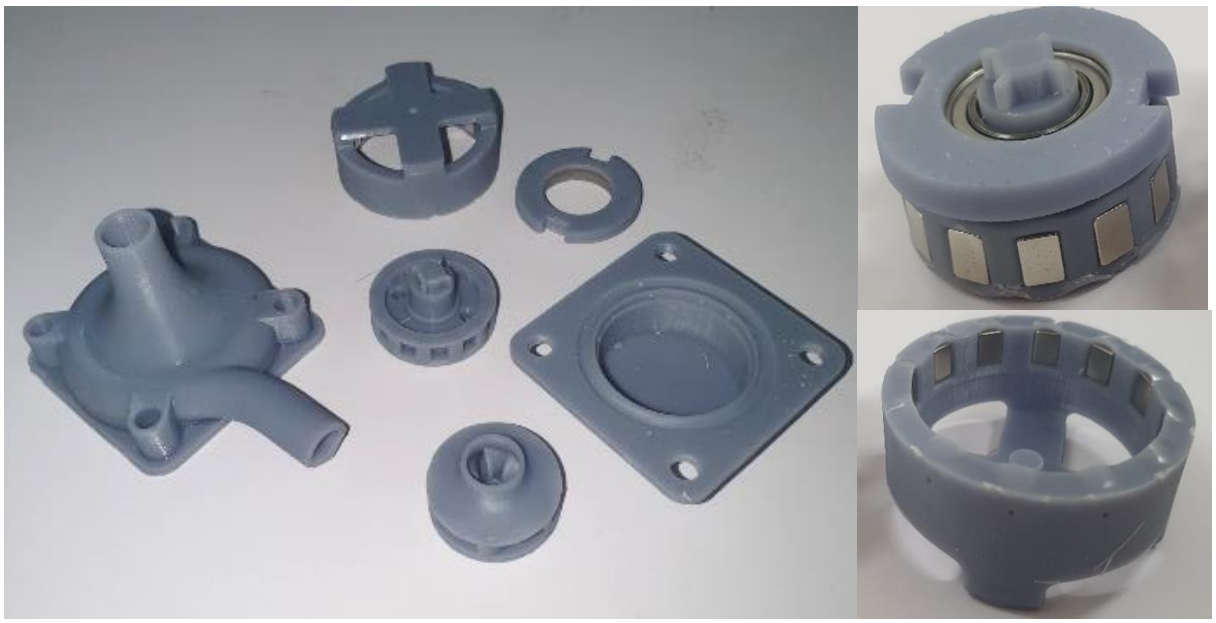

Figure 17 3-D printed parts and the assembled magnets components

III.4 Conclusion

In summary, the magnetic coupling was successfully designed and validated through rigorous FEM simulation, demonstrating a maximum transmissible torque of 0.102 N·m, which far exceeds the operational requirement. This robust design ensures reliable, slip-free power transmission under all anticipated operating conditions. Furthermore, the chapter detailed the successful fabrication of all necessary pump components using ABS-like resin and 3D printing technology. This confirms the manufacturability of the design and produces the physical parts required for assembly and experimental testing.

CHAPTER IV:
EXPEIMENTAL SETUP, RESULTS AND DISSCUSSION

IV.1 Introduction

Following the successful design and fabrication of the pump, this chapter transitions from the theoretical and simulation phases to physical validation. It describes the experimental setup constructed to test the performance of the 3D-printed prototype. The methodology for data acquisition is detailed, outlining how key parameters such as flow rate and pressure are measured across a range of operating speeds controlled by varying the input voltage. The objective is to empirically evaluate the pump's hydraulic performance and compare it against the initial design expectations.

IV.2 Experimental Setup

Figure 18 shows the synoptic scheme of the experimental setup

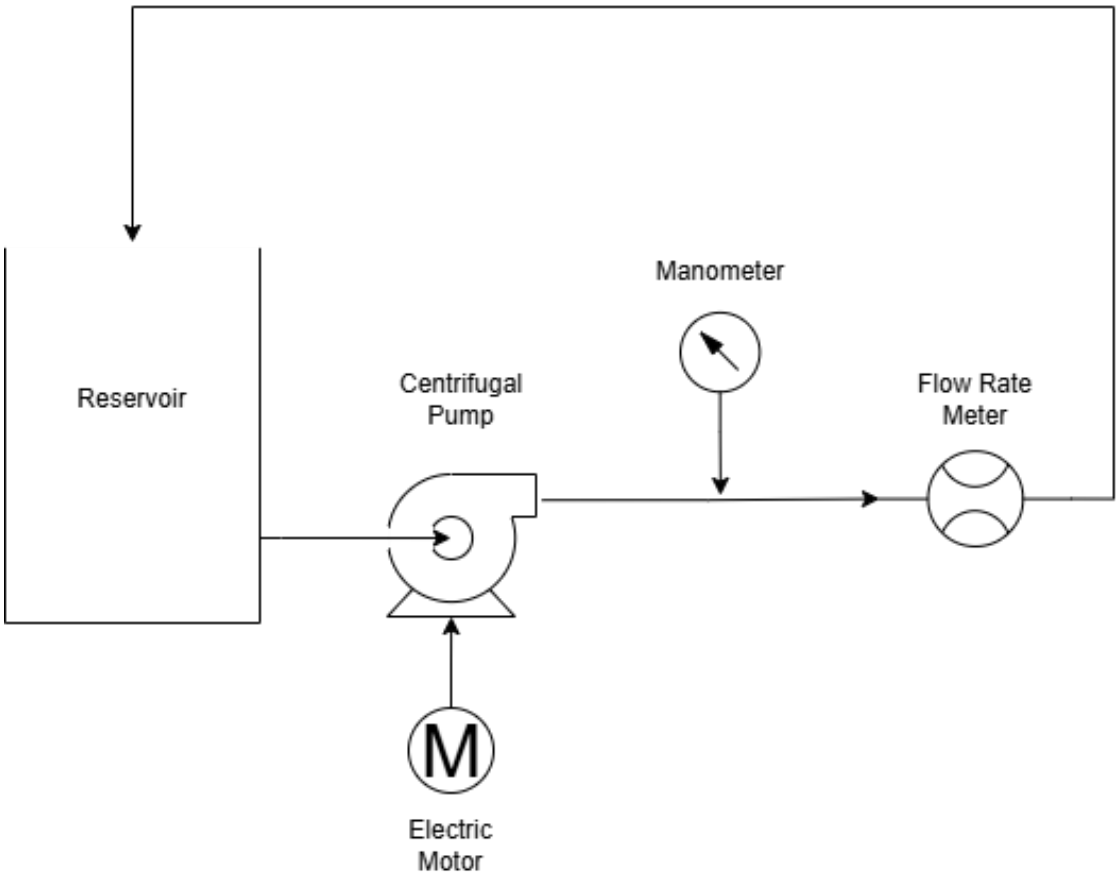

Figure 18 Synoptic scheme of the experimental setup

Main Components:

- A reservoir
- A centrifugal pump driven by an electric motor (M)
- A manometer for pressure measurement.
- A flow rate meter at the discharge end.

Fluid flows from the reservoir through the centrifugal pump, past the manometer (which measures the pressure at that point), and through the flow rate meter which quantifies the volumetric flow rate providing real-time flow rate data.

The experimental equipment is demonstrated in Figure 18, for testing the performances of the 3D-printed pump (6) by adjusting supply voltage using a DC Power supply (2), resulting in a change rotation speed (RPM) using an infrared tachometer (1). Then we proceed to take measurements of the flow rate and the pressure developed by the pump and note the observations taken. In order to provide repeatability and enhance accuracy within our experiments, we utilized a precision electronic flow meter (4) and a corresponding VDAS type data acquisition system and kept the level of water in the reservoir (3) steady in all experiments, while pressure is being measured by the utilization of an electronic manometer (5) with a range of up to ±2000 mBar.

Figure 19 Experimental setup equipment

Rotation speed was measured before the experience with varying the voltage and measuring the rotation speed at the tip of the impeller which gives us the following results in Table 10:

Table 12 Rotation speed at various voltage values

Voltage [V]	Revolutions per minute
4	1110
5	1412
6	1766
7	2103
8	2450
9	2823
10	3290
11	3660
12	3990

IV.3 Results and Discussion

Flow rate

The following graph (Figure 20) shows the flow rate results obtained from our experimental setup:

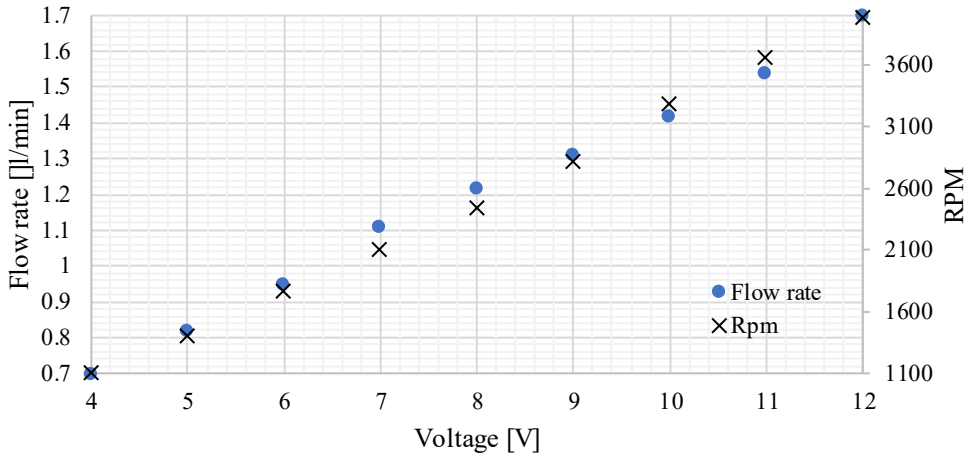

Figure 20 Flow rate results of the pump

The plot of flow rate against voltage in Figure 19 illustrates a linear and positive relationship between the two parameters. As the voltage applied across the DC motor of the pump increases from 4 V to 12 V, the flow rate increases steadily from around 0.7 L/min to 1.7 L/min. This is to be anticipated, and an increased voltage increases the speed of rotation (RPM) of the motor, as evident from Table 10 of the thesis. This increased impeller speed provides more kinetic energy to the fluid and thus the increased volumetric output. This experimentally validates the ability of the pump to regulate flow by varying the input voltage, which is a major requirement in most microfluidic devices.

Pressure

The following graph (Figure 21) shows the pressure results obtained from our experimental setup:

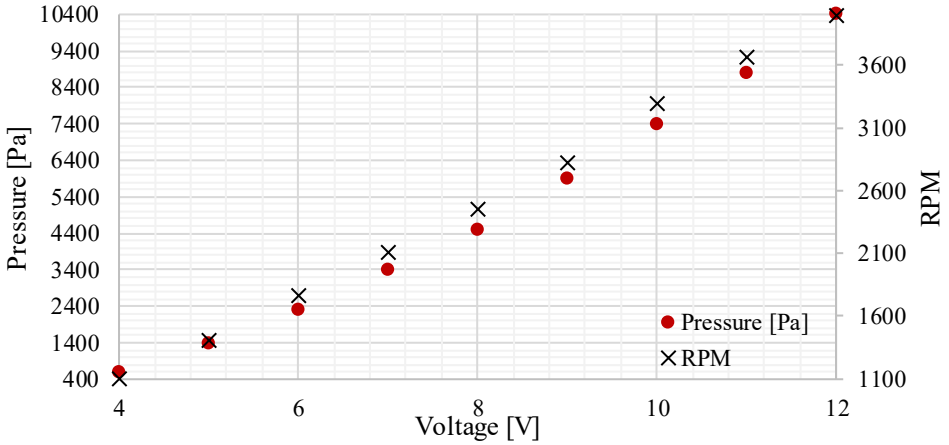

Figure 21 Pressure result of the pump

In the same manner, the pump's pressure output in Figure 20 is also in strong positive correlation with the voltage input. The plot shows that as voltage increases from 4 V to 12 V, the pressure created by the pump increases from a low level to above 10,000 Pa (10 kPa). This is in line with

basic principles of centrifugal pumps, where head (and hence pressure) is directly proportional to the rotational speed of the impeller squared. The experimental findings, thus, validate that the speeding up of the motor by increasing the voltage results in a large enhancement of the pressure head pumpable by the pump. The pressures measured are of the same order of magnitude as the estimated pressure increase from the initial design calculations (about 3.9 kPa at 2500 RPM) and the CFD simulation (4886 Pa at 2500 RPM).

F*low coefficient and Head coefficient*

The following graph in Figure 22 shows the calculated head coefficient and flow coefficient of the pump

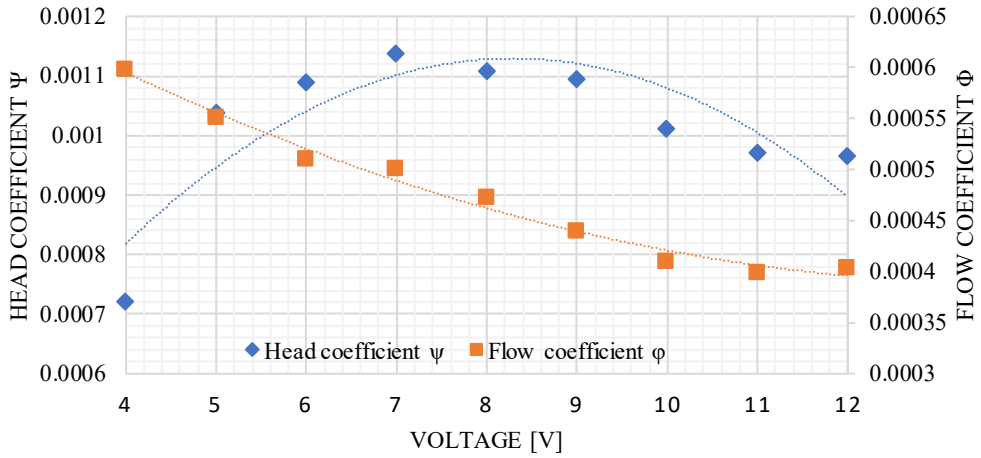

Figure 22 Flow coefficient and Head coefficient results of the pump

This plot illustrates the non-dimensional performance of the pump by graphing the head coefficient (ψ) and the flow coefficient (ϕ) versus the input voltage and with the trend line shown as dashed lines.

Flow Coefficient (ϕ): Flow coefficient, quantifying the flow capacity of the pump in relation to its size and velocity, follows a general declining trend with increasing voltage from 4V to 12V. This means that although the actual flow rate is higher at higher voltages (as observed from the first graph), the rate of increase relative to the impeller tip speed decreases at higher RPMs.

Head Coefficient (ψ): The head coefficient, i.e., energy transferred to the fluid with respect to tip speed of impeller, is a parabolic function. It rises with voltage, peaks at approximately 8-9 V, and then starts to decline. This peak represents the Best Efficiency Point (BEP) for the range tested, at which the pump is most efficient at converting the motor's mechanical energy to fluid energy (head). Pump operation at the voltage that yields the peak head coefficient will likely result in the highest hydraulic efficiency for these test conditions.

Collectively, these plots illustrate a thorough experimental verification of the operation of the 3D-printed mini centrifugal pump, validating the anticipated inter relationships among flow rate, pressure, and motor speed, and determining an optimal operating range from the computed hydraulic coefficients, while the optimal working point would preferably be the intersection between the two lines.

IV.4 Performance comparison

A previous study was conducted with the same setup as well as the same motor using a different pump design and a different magnetic coupling method, its performances were compared to the new pump designed in this study and the results are shown in figure 24:

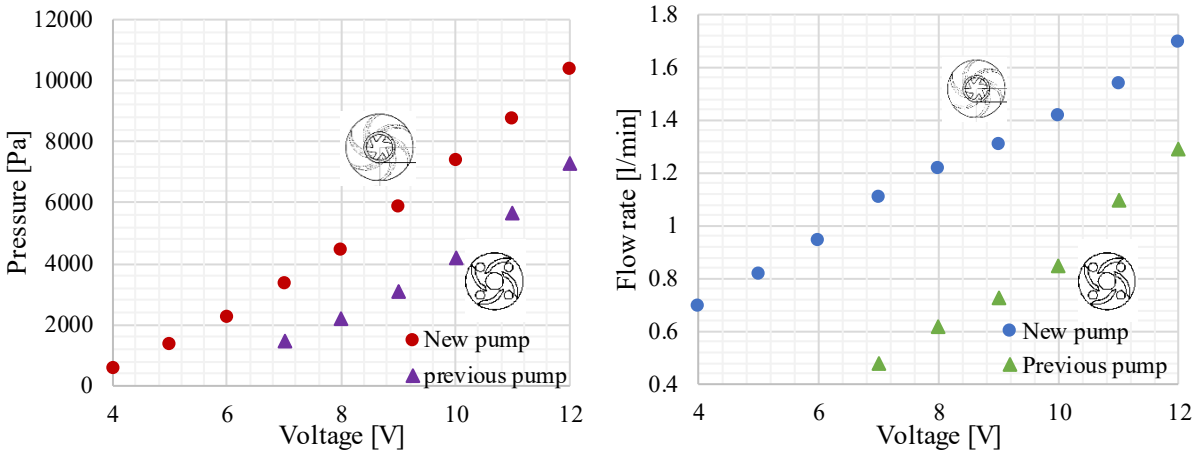

Figure 23 Flow rate and pressure comparison of the new and previous pumps

The results show significant performance enhancement in the new pump compared to the previous version. The graphs plot pressure and flow rate against operating voltage, and in both cases, the new pump consistently outperforms the previous pump across the entire voltage range with a calculated **11%** average increase of rotation speed when applying the same voltage as well as **74%** average increase in flow rate and **84%** average increase in pressure, indicating that the design optimizations and new magnetic coupling method were highly effective.

IV.5 conclusion

In conclusion, the experimental results effectively demonstrate the operational capabilities of the manufactured miniature centrifugal pump. The data confirms a direct and predictable relationship between input voltage, flow rate, and the pressure head generated. Analysis of the non-dimensional head and flow coefficients revealed the pump's characteristic performance curve and identified an optimal operating range around 8-9V for peak efficiency with significant improvement over the old pump performance. These findings validate the functionality of the design and fabrication process, providing a solid empirical basis for the overall assessment of the pump's performance.

CONCLUSION AND FUTURE WORK

This engineering thesis in Energy and Sustainable Development addresses the challenge of enhancing the performance of miniaturized centrifugal pumps, which are increasingly critical in high-precision applications such as biotechnology, microfluidics, and electronics cooling. These systems demand compact, leak-proof, and energy-efficient fluid handling solutions—needs often constrained by traditional manufacturing methods and limited torque transmission mechanisms. To overcome these limitations, this project proposed an integrated development approach combining innovative design, multiphysics simulation, and additive manufacturing.

The objective was to design, fabricate, and experimentally validate a compact 3D-printed centrifugal pump with a seal-less architecture, enabled by a synchronous magnetic coupling. The hydraulic geometry of the pump was first defined using CFturbo and SolidWorks, ensuring compatibility with design constraints and performance targets. A twofold simulation process was then employed: Computational Fluid Dynamics (CFD) using ANSYS Fluent was used to analyze internal flow behavior and estimate the impeller's operating torque (0.00475 N·m), while Finite Element Modeling (FEM) via COMSOL Multiphysics was applied to evaluate the magnetic coupling. Simulations confirmed the magnetic assembly could transfer a torque of up to 0.102 N·m, offering a robust and slip-free power transmission with a safety factor greater than 10.

After virtual validation, the pump components were fabricated using an Anycubic Photon Mono 4K printer with ABS-like resin, demonstrating the feasibility of using resin-based 3D printing for producing complex, miniature pump geometries. The integration of the magnetic rotor within the printed casing was achieved with precision, minimizing slip (measured detachment angle ≈ 15° for 12 poles) and maintaining assembly compactness. Experimental testing showed a maximum flow rate of 1.7 L/min and pressure up to 10 kPa at 12 V, closely matching theoretical predictions ($\Delta p \approx 3.9$ kPa at 2500 RPM). Overall pump efficiency was measured at 23%, compared to a theoretical value of 36%, with minor losses attributed to surface roughness (≈20 μm) and friction unaccounted for in idealized CFD assumptions.

Most significantly, the newly optimized pump demonstrated an 84% increase in pressure and a 74% increase in flow rate compared to a previous design under similar operating conditions. These gains validate the chosen optimization strategy and highlight the effectiveness of the integrated design and fabrication process.

While the project achieved its goals, several avenues for improvement were identified: refining rotor-holder alignment to reduce friction, exploring high-performance engineering polymers with superior chemical and mechanical properties, and enhancing measurement accuracy through better sensors and automated data logging. Additionally, future iterations may focus on reducing part count, simplifying assembly, and further miniaturizing the pump to extend its applicability.

In conclusion, this work represents a complete and successful development cycle, from conceptual design to physical validation, of a high-performance miniature pump. The synergistic use of CFD, FEM, and 3D printing not only enabled rapid prototyping but also demonstrated a scalable methodology for developing next-generation microfluidic devices. This hybrid approach lays a strong foundation for patentable innovations with real industrial and technological impact.

REFRENCES

[1] J. Tuzson, *CENTRIFUGAL PUMP DESIGN*, 1st Edition. New York, USA: John Wiley & Sons, Inc., 2000.

[2] B. Jo, Y. Morimoto, and S. Takeuchi, "3D-Printed Centrifugal Pump Driven by Magnetic Force in Applications for Microfluidics in Biological Analysis," *Adv Healthc Mater*, vol. 11, no. 24, Dec. 2022, doi: 10.1002/adhm.202200593.

[3] M. Zhou *et al.*, "Miniaturized soft centrifugal pumps with magnetic levitation for fluid handling," 2021. [Online]. Available: https://www.science.org

[4] X. Wang, C. Cheng, S. Wang, and S. Liu, "Electroosmotic pumps and their applications in microfluidic systems," 2009. doi: 10.1007/s10404-008-0399-9.

[5] I. Ederer, P. Raetsch, W. Schullerus, C. Tille, and U. Zech, "sENds NI A RS A ELSEVIER Sensors and Actuators A 62 (1997) 752-755 Piezoelectrically driven micropump for on-demand fuel-drop generation in an automobile heater with continuously adjustable power output," 1997.

[6] C. F. Lieu, W. K. Chan, and K. T. Ooi, "Experimental investigation of the reciprocating ball pump (RBP)," *Med Eng Phys*, vol. 34, no. 8, pp. 1101–1108, Oct. 2012, doi: 10.1016/j.medengphy.2011.11.016.

[7] "zengerle1995".

[8] "Section TECH-A Centrifugal Pump Fundamentals."

[9] S. Taguchi, R. Yozu, A. Mori, T. Aizawa, and S. Kawada, "A Miniaturized Centrifugal Pump for Assist Circulation," Blackwell Science. Inc.

[10] D. P. Sloteman and M. Piercey, "Developing Sealless Integral Motor Pumps Using Axial Field, Permanent Magnet, Disk Motors," *the 17th International Pump Users Symposium*, 2000.

[11] A. Rossetti, G. Pavesi, and G. Ardizzon, "A new two stage miniature pump: Design, experimental characterization and numerical analyses," *Sens Actuators A Phys*, vol. 164, no. 1–2, pp. 74–87, Nov. 2010, doi: 10.1016/j.sna.2010.09.003.

[12] D. Kearney, R. Grimes, and J. Punch, "An experimental investigation of the flow fields within geometrically similar miniature-scale centrifugal pumps," *Journal of Fluids Engineering, Transactions of the ASME*, vol. 131, no. 10, pp. 1011011–10110110, Oct. 2009, doi: 10.1115/1.3176985.

[13] S. Liu, M. Nishi, and K. Yoshida, "Impeller geometry suitable for mini turbo-pump," *Journal of Fluids Engineering, Transactions of the ASME*, vol. 123, no. 3, pp. 500–506, 2001, doi: 10.1115/1.1385385.

[14] S. Ugaki *et al.*, "Efficacy of a miniature centrifugal rotary pump (TinyPump) for transfusion-free cardiopulmonary bypass in neonatal piglets," *ASAIO Journal*, vol. 53, no. 6, pp. 675–679, Nov. 2007, doi: 10.1097/MAT.0b013e3181590719.

[15] Y. Wu, H. Yuan, J. Shao, and S. Liu, "Experimental Study on Internal Flow of a Mini Centrifugal Pump by PIV Measurement."

[16] M. Cong and K. Liu, "Recent Patents in Magnetic Transmission and Applications," 2010.

[17] M. Schilling, “Dexter Magnetic Technologies Magnetic Couplings in Medical Device Applications Magnetic Couplings in Medical Device Applications An Overview of Magnetic Technology in Medical Devices.” [Online]. Available: www.dextermag.com

[18] İ. Özkul, C. Aksu Canbay, and E. Engüzel, “Synchronous and Asynchronous Magnetic Couplings: A Comparative Study on Operating Principles, Advantages, and Industrial Applications,” 2024.

[19] R. B. Bronzeri and I. E. Chabu, “Concept Validation of an Automotive Variable Flow Water Pump with an Eddy Current Magnetic Coupling,” *IEEE Transactions on Transportation Electrification*, vol. 7, no. 4, pp. 2939–2950, Dec. 2021, doi: 10.1109/TTE.2021.3075648.

[20] J. fang LIU, H. Choi, and M. Walmer, “Design of Permanent Magnet Systems Using Finite Element Analysis,” *Journal of Iron and Steel Research International*, vol. 13, no. SUPPL. 1, pp. 383–387, 2006, doi: 10.1016/S1006-706X(08)60214-9.

[21] E. P. Furlani, R. Wang, and H. Kusnadi, “A Three-Dimensional Model for Computing the Torque of Radial Couplings,” *IEEE Trans Magn*, vol. 31, no. 5, pp. 2522–2526, 1995, doi: 10.1109/20.406554.

[22] L. Joswig, M. J. Vellekoop, and F. Lucklum, “Miniature 3D-printed centrifugal pump with non-contact electromagnetic actuation,” *Micromachines (Basel)*, vol. 10, no. 10, Oct. 2019, doi: 10.3390/mi10100631.

[23] T. H. Yusanto, J. Julian, F. Wahyuni, A. Winarta, and W. M. Managi, “Design and Performance Testing of a 3D Printed Mini DC Powered Pump for Microbubble Generator,” 2023.

[24] S. R. Shah, S. V. Jain, R. N. Patel, and V. J. Lakhera, “CFD for centrifugal pumps: A review of the state-of-the-art,” in *Procedia Engineering*, Elsevier Ltd, 2013, pp. 715–720. doi: 10.1016/j.proeng.2013.01.102.

[25] P. V. Patil, D. S. Pawar, C. S. Mote, A. B. Deshmukh, and S. V. Jadhav, “Design, Fabrication, and Analysis of Miniature Centrifugal Pump,” *International Journal of New Technology and Research*, vol. 5, no. 4, Apr. 2019, doi: 10.31871/ijntr.5.4.35.

APPENDICES

Appendix A: Components Technical Drawings

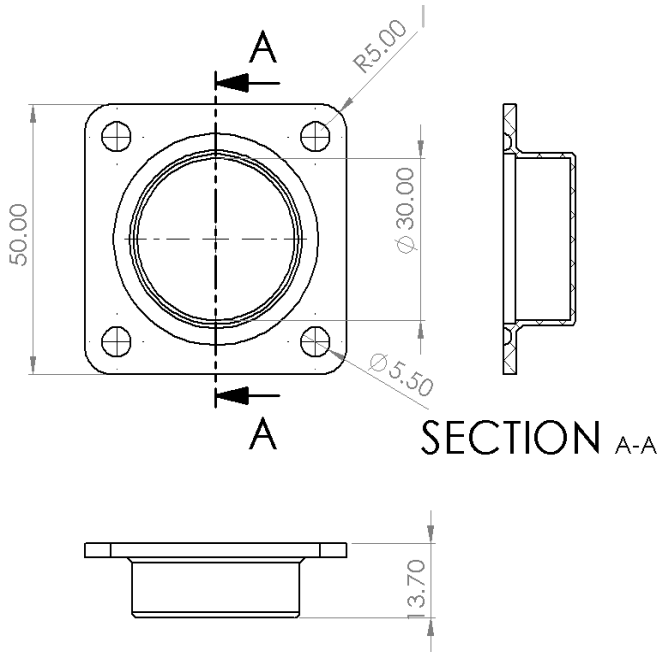

Figure 24 Case

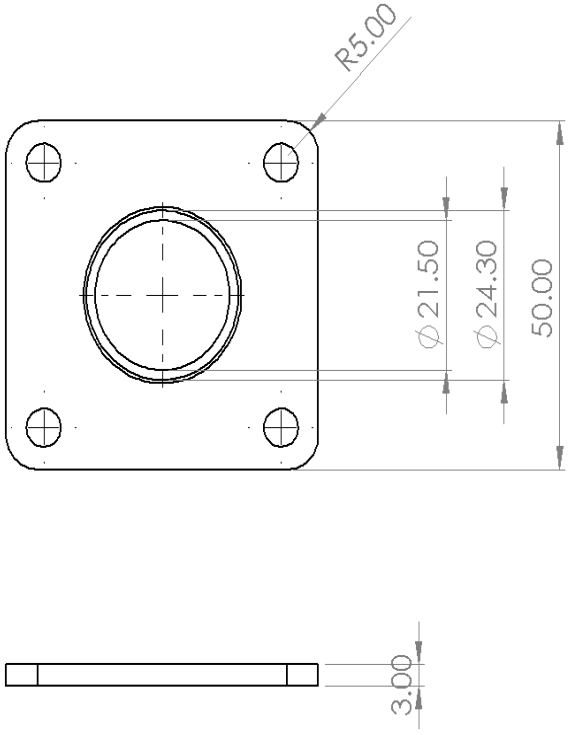

Figure 25 Motor Holder

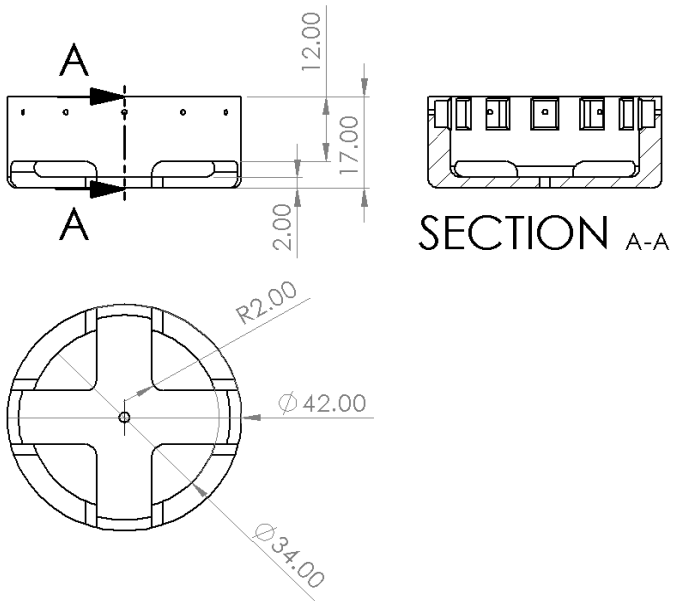

Figure 26 Rotor

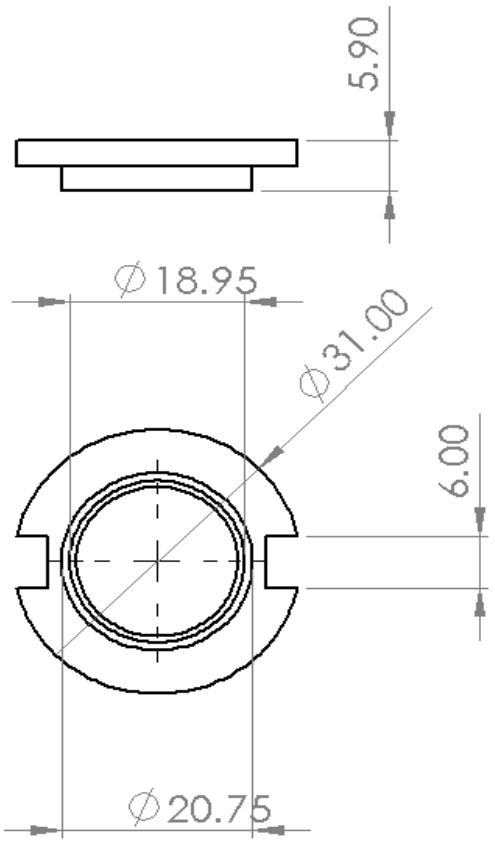

Figure 27 Cover

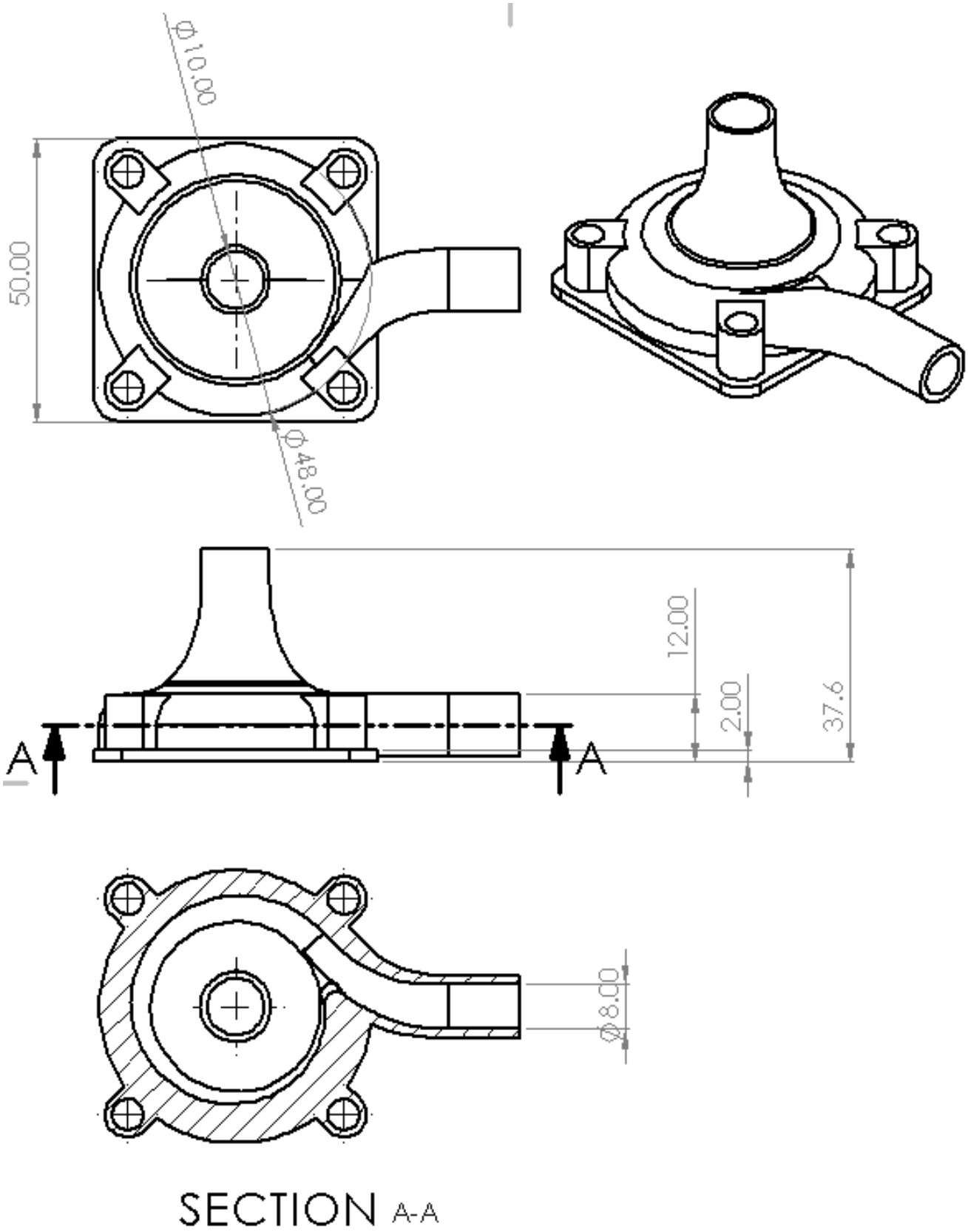

Figure 28 Volute

Appendix B: Torque Analysis Using CFD Simulation

This section presents the Computational Fluid Dynamics (CFD) analysis carried out using ANSYS Fluent to validate the hydraulic design of the miniature magnetically coupled centrifugal pump. The CFD study not only provides key performance metrics (head, flow rate, efficiency) but also yields the impeller torque—an essential parameter for sizing the magnetic coupling.

B.1 CFD Methodology

Geometry Preparation and Meshing Strategy

The hydraulic geometry, including the impeller and volute, was initially designed in **CFturbo**. One of its advantages is the generation of clean, simulation-ready geometry with pre-labeled domains. The entire model was exported in STEP format and imported into **ANSYS SpaceClaim** for final preparation.

Once in ANSYS, the model was transferred to **Fluent Meshing**, where the mesh was generated:

- **Minimum Element Size**: 0.25 mm, based on sensitivity analysis of the mesh.
- **Meshing Technique**: **Poly-Hexcore Mesh**, leveraging the advantages of hex-core volumes for bulk flow and polyhedral elements near complex surfaces.
- **Boundary Layer Resolution**: Inflation layers were added along walls to capture near-wall effects and support turbulence modeling accuracy.
- **Mesh Quality**: Skewness and orthogonality (average of 0.91) were monitored to ensure mesh quality remained within acceptable limits (maximum skewness < 0.85).

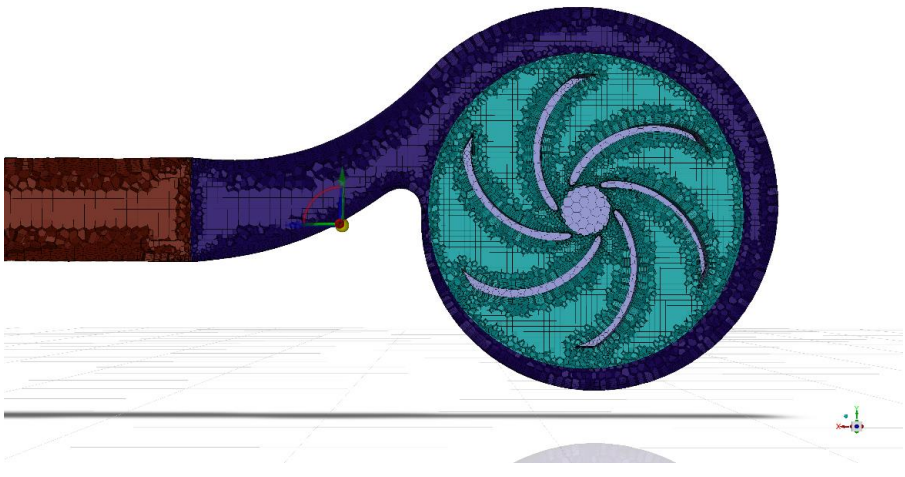

Figure 29 mesh result of the pump

This meshing methodology ensured a balance between computational efficiency and result accuracy.

Physics Setup

The CFD setup mirrored real operating conditions to allow direct validation of the hydraulic design and extraction of dynamic parameters for magnetic coupling design.

Table 13 physics setup of the CFD simulation

Parameter		Setting
Solver		Pressure-based, steady-state, 3D, incompressible flow
Fluid		Water at 25°C
Turbulence Model		*k-ω SST* (Shear Stress Transport)
Rotational Frame		Rotating reference frame applied to the impeller domain
Rotational Speed		2500 rpm
Boundary conditions	Inlet	Pressure inlet at atmospheric pressure (0 Pa gauge)
	Outlet	Pressure outlet
	Walls	No-slip boundary conditions; impeller blades treated as rotating walls

B.2 CFD Simulation Results

Performance Prediction

The CFD simulation provided the complete hydraulic performance of the pump at the design operating point. The key metrics obtained include:

Table 14 key performance results of the pump

Parameter	Value
Outlet Pressure	4886 Pa
Flow Rate	2.2 L/min
Outlet Velocity	1.25 m/s
Impeller Torque	0.00475 Nm

Internal Flow Analysis

To evaluate the quality of the flow and detect any potential performance-degrading phenomena, contour plots and vector fields were analyzed:

Pressure Contours

The pressure contour analysis reveals characteristic centrifugal pump pressure distribution with pressure ranging from 1.47×10^{3} Pa to 1.00×10^{4} Pa, showing the expected pressure field for rotating machinery. The visualization displays a distinct low-pressure region (blue) at the impeller eye/center due to suction effects created by the centrifugal action, which draws fluid into the pump center. From this low-pressure core, the pressure increases radially outward through the impeller passages as the rotating blades add energy to the fluid, reaching maximum values (red) at the volute periphery and discharge. The characteristic spiral pressure pattern within the impeller demonstrates proper centrifugal action with effective momentum transfer, while the pressure gradient from the suction eye to the volute outlet confirms the pump's ability to generate head. The gradual pressure recovery in the volute chamber indicates good diffusion performance, and the smooth pressure transitions suggest stable operation with minimal flow separation that could compromise performance.

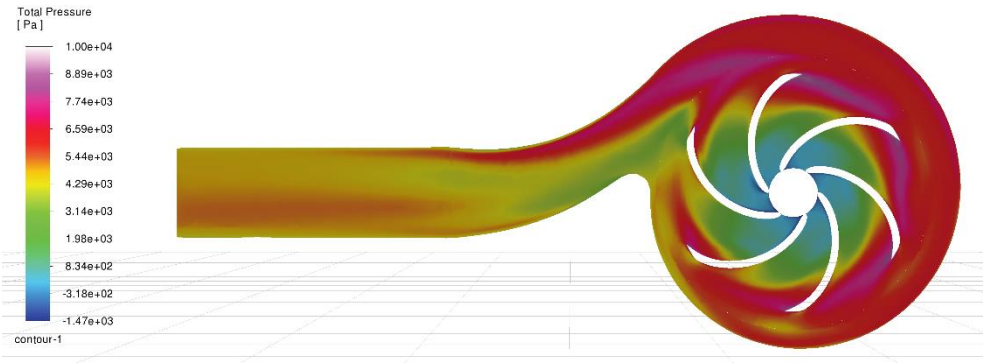

Figure 30 pressure contour

Velocity Contours :

The velocity magnitude distribution demonstrates typical centrifugal pump flow characteristics with velocities ranging from near-zero at the suction inlet to maximum values of 3.60 m/s at the impeller blade tips. The low inlet velocities (~0.36 m/s) gradually accelerate through the impeller passages, reaching peak values at the impeller periphery consistent with the rotational motion and centrifugal acceleration. The high-velocity regions (red) at the impeller exit indicate effective kinetic energy impartation to the fluid, while the subsequent velocity reduction through the volute chamber demonstrates proper kinetic-to-pressure energy conversion. The smooth velocity transitions across the impeller channels suggest balanced design with uniform flow distribution, and the gradual deceleration from impeller exit to volute outlet confirms effective diffusion performance. The maximum tip velocity of 3.60 m/s is appropriate for the 2500 RPM operating speed, indicating reasonable mechanical stress levels and acceptable hydraulic loading.

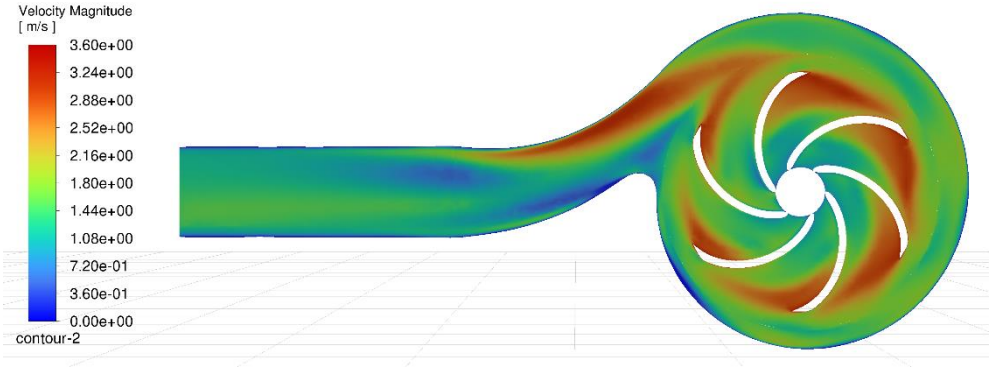

Figure 31 velocity contour

Turbulence Streamlines

The turbulence intensity analysis reveals complex flow patterns with intensity levels ranging from 5.28×10^{-2} % to 3.67×10^{1} %, concentrated primarily in the impeller wake regions and volute tongue area where flow interactions are most pronounced. The 3D streamlines illustrate the intricate secondary flow patterns, including recirculation zones and vortical structures that develop due to the interaction between the impeller discharge flow and the volute geometry.

Higher turbulence intensities (yellow-red regions exceeding 20%) are observed behind the impeller blade trailing edges and at the volute tongue where the rotating impeller flow meets the stationary volute, creating shear layers and flow mixing. While these turbulent regions indicate energy dissipation and potential efficiency losses, the overall moderate turbulence levels suggest stable pump operation without severe flow breakdown or excessive hydraulic losses. The streamline patterns reveal areas where geometric optimization could reduce turbulence intensity, particularly in the volute tongue region and blade exit geometry, which could enhance overall pump efficiency and reduce noise and vibration levels.

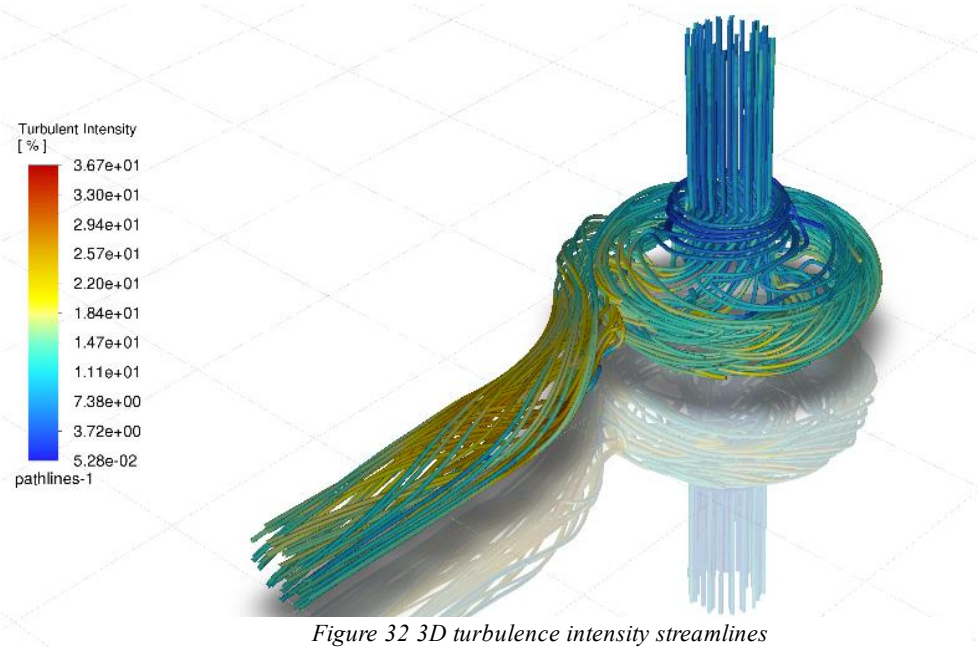

Figure 32 3D turbulence intensity streamlines

Impeller Torque Calculation

One of the most critical outcomes of this simulation is the **impeller torque** (moment), as it directly determines the strength of the magnetic coupling required.

Using Fluent's moment calculation on the rotating domain, the **torque value** was extracted from the z-axis (rotational axis).

This result served as the direct input for the **COMSOL Multiphysics** study to design the permanent magnet arrangement ensuring that the coupling can handle the worst-case dynamic load with sufficient safety and rotational inertia.

B.3 Conclusion

The CFD simulation confirmed that the pump performs as expected at 2500 rpm and atmospheric inlet pressure. The obtained head, flow rate, and efficiency matched the design targets, while the torque data provided the foundation for magnetic coupling design. No critical flow separation was observed, validating the hydraulic configuration developed in CFturbo.